B 5 Scattering Techniques II: Magnetic X-Ray Scattering

Th. Brückel
Institut für Festkörperforschung
Forschungszentrum Jülich GmbH

Contents

1 Introduction

Most of our present knowledge of the atomic structure of condensed matter results from x-ray diffraction studies, which probe the interaction of the electric field with the electric charge of the electron. However, since x-rays represent an electro*magnetic* radiation and since in magnetic materials some electrons carry a magnetic moment due to spin- and angular momentum, we naturally would expect a magnetic interaction in addition to the pure charge interaction. Even so this interaction was well established in theory [1] since Klein-Nishina 1929, the first magnetic diffraction effect was demonstrated only 1972 by de Bergevin and Brunel [2] with a commercial x-ray tube. The same authors gave a classical picture of the interaction process, deduced the detailed polarisation dependence and presented measurements on ferromagnetic compounds in a subsequent paper [3]. However, since the magnetic interaction gives just a relativistic correction to the cross section, the amplitudes of magnetic diffraction are down by approximately three orders of magnitude as compared to charge scattering, resulting in an intensity ratio of about 10^{-6}. Therefore magnetic x-ray scattering was considered an exotic topic until the experiments on Ho by Gibbs et al. [4], which took advantage of the high brilliance of a synchrotron radiation x-ray source thus compensating by a high photon flux at the sample position for the weak magnetic scattered intensities. The polarisation properties and the tunability of synchrotron radiation offered new perspectives for magnetic x-ray investigations. This was again demonstrated on Ho [5] by an attempt to separate spin- and angular momentum with polarisation analysis and by the observation of a resonance enhancement of the magnetic signal at the absorption edges.

Nowadays, synchrotron radiation techniques for the study of properties of magnetic materials are well established. Very widespread is the application of incoherent probes which measure a macroscopic ensemble average of local magnetic properties. Among these we mention Kerr-microscopy, measurements of the Faraday effect and the linear or circular x-ray magnetic dichroism. The Kerr- and Faraday effect measure the rotation of the plane of polarisation of an electromagnetic wave as it is reflected from or transmitted through a magnetic material, respectively. Magnetic circular dichroism describes the difference in the absorption of right- and left circularly polarised x-rays by magnetic materials. It measures essentially the same quantities as the Kerr- and Faraday effect, namely the orbital and spin contributions to the magnetic moments with element and certain site specifities. Kerr microscopy and x-ray topography are used for magnetic domain imaging. Absorption techniques become local microscopic probes when the spin resolved x-ray absorption fine structure is observed. In analogy to classical EXAFS experiments, such measurements provide information about the local environment, but are explicitly sensitive to the magnetic neighbours only. True microscopic spatial resolution is obtained with the coherent probes, namely magnetic x-ray diffraction (as well non-resonant as resonance exchange scattering) and nuclear resonant scattering. Magnetic scattering provides a wealth of information on magnetic correlation lengths, the local magnetic moments and environment, the magnetic structure and phase transitions. Magnetic x-ray reflectivity is the corresponding probe for the investigation of magnetic thin films. Nuclear resonant scattering yields information on hyperfine fields and might eventually become important for the measurement of magnetic excitations. Resonant diffraction and absorption techniques are intimately related by the optical theorem, which states that the attenuation coefficient is proportional to the imaginary part of the forward scattering amplitude. In this sense, diffraction experiments comprise absorption techniques, but in addition they provide true atomic resolution. In this impressive list of synchrotron radiation techniques we want to finally mention magnetic Compton scattering for the determination of the spin resolved electron momentum density and angular- and spin resolved photoemission, which gives the spin resolved band structure.

Many of these topics are discussed in detail in a textbook [6]. In what follows I will concentrate on magnetic x-ray diffraction. I will introduce the cross section for non-resonant and resonant magnetic x-ray scattering in section 2 and discuss experimental considerations in section 3. Examples of resonance exchange scattering experiments on bulk antiferromagnets, ferromagnets and thin film systems are given in section 4. Section 5 gives some examples for non-resonant x-ray scattering, before we summarise in section 6 some important features of magnetic x-ray scattering and compare it to magnetic neutron diffraction.

2 The cross section for magnetic x-ray scattering

A calculation of the cross-section for x-ray scattering including the magnetic terms from a quasi-relativistic Hamiltonian for electrons in a quantised electromagnetic field within second-order perturbation theory was done by Blume [7] and Blume and Gibbs [8]. Platzman and Tzoar [1] and de Bergevin and Brunel [3] started from the Dirac equation and reduced this relativistic ansatz using a Foldy-Wouthuysen transformation to a quasi-non-relativistic form analogous to that obtained from the non-relativistic Hamiltonian. The expansion of this quasi-non-relativistic Hamiltonian in dependence of photon energy over electron rest mass $\hbar\omega / mc^2$ allows the description of the magnetic scattering process. Grotch, Kazes, Bhatt and Owen [9] extended the Foldy-Wouthuysen transformation to second order in $\hbar\omega / mc^2$. Here we follow a presentation given by Blume [7] and Blume and Gibbs [8] based on a non-relativistic treatment in second order perturbation theory. We start with the Hamiltonian for electrons in a quantised electromagnetic field:

$$\begin{aligned}\mathbf{H} = {} & \sum_j \frac{1}{2m}(\underline{\mathbf{P}}_j - \frac{e}{c}\underline{\mathbf{A}}(\underline{\mathbf{r}}_\mathrm{j}))^2 + \sum_{ji}\mathbf{V}(\mathbf{r}_\mathbf{ij}) - \frac{e\hbar}{mc}\sum_j \underline{\mathbf{s}}_\mathrm{j}\cdot\underline{\nabla}\times\underline{\mathbf{A}}(\underline{\mathbf{r}}_\mathrm{j}) \\ & - \frac{e\hbar}{2(mc)^2}\sum_j \underline{\mathbf{s}}_\mathrm{j}\cdot\underline{\mathbf{E}}(\underline{\mathbf{r}}_\mathrm{j})\times(\underline{\mathbf{P}}_\mathrm{j} - \frac{e}{c}\underline{\mathbf{A}}(\underline{\mathbf{r}}_\mathrm{j})) + \sum_{k\lambda}\hbar\omega_k(\mathbf{c}^+(\underline{\mathbf{k}}\boldsymbol{\lambda})\mathbf{c}(\underline{\mathbf{k}}\boldsymbol{\lambda}) + \frac{1}{2})\end{aligned} \qquad (1)$$

Here, the first term corresponds to the kinetic energy of the electrons in the electromagnetic field, represented by the vector potential $\underline{\mathbf{A}}(\underline{\mathbf{r}})$, the second term corresponds to the Coulomb interaction between the electrons, the third term to the Zeeman energy $-\underline{\mu}\cdot\underline{H}$ of the electrons with spin $\underline{s}_j$, the fourth term to the spin-orbit coupling and the final term to the self energy of the electromagnetic field. From the form of (1), we can immediately guess that the cross-section and polarisation dependence of the scattering of an electromagnetic wave from magnetic materials is more complex than the corresponding cross-section for neutron scattering - at least if we only consider the two main interaction potentials for nuclear scattering and magnetic dipole scattering. In the case of neutron scattering, only the magnetic dipole interaction of the neutron spin with the magnetic field of the electrons gives rise to magnetic scattering. In the case of x-rays, we have several interaction terms as well between the spin of the electrons and the electromagnetic field as between the orbital momentum and the magnetic field. In addition, photons are spin 1 particles as compared to spin 1/2 neutrons. Therefore we can expect a much more complex polarisation dependence.

The vector potential $\underline{\mathbf{A}}(\underline{\mathbf{r}})$ in (1) is linear in photon creation and annihilation operators, $\mathbf{c}^+(\underline{\mathbf{k}}\boldsymbol{\lambda})$ and $\mathbf{c}(\underline{\mathbf{k}}\boldsymbol{\lambda})$ and is given in a plane wave expansion by:

$$\underline{\mathbf{A}}(\underline{\mathbf{r}}) = \sum_{\underline{q}\sigma} \left(\frac{2\pi\hbar c^2}{V\omega_q} \right)^{\frac{1}{2}} \times [\underline{\varepsilon}(\underline{q}\sigma)\mathbf{c}(\underline{\mathbf{q}}\boldsymbol{\sigma})e^{i\underline{q}\cdot\underline{r}} + \underline{\varepsilon}^*(\underline{q}\sigma)\mathbf{c}^+(\underline{\mathbf{q}}\boldsymbol{\sigma})e^{-i\underline{q}\cdot\underline{r}}] \qquad (2)$$

Here V is a quantisation volume and $\underline{\varepsilon}(\underline{q}\sigma)$ is the unit polarisation vector corresponding to a wave with wavevector $\underline{q}$ of polarisation state σ. Two polarisation states $\sigma = 1,2$ of the photons have to be distinguished. As a basis, we can either use linear polarisation in two perpendicular directions or left and right circular polarisation. Since $\underline{\mathbf{A}}(\underline{\mathbf{r}})$ is linear in the $\mathbf{c}^+$ and **c**-operators, scattering occurs in second order for terms linear in $\underline{\mathbf{A}}$ and in first order for quadratic terms. We do not want to reproduce the calculation given in [7] in detail. The Hamiltonian (1) is written as a sum

$$\mathbf{H} = \mathbf{H_0} + \mathbf{H_r} + \mathbf{H'} \qquad (3)$$

where $\mathbf{H_0}$ contains only the degrees of freedom of the electron system, $\mathbf{H_r}$ is the Hamiltonian for the quantised electromagnetic field and **H'** corresponds to the interaction between the electrons and the radiation field. Scattering cross-sections are calculated by assuming that initially the solid is in a quantum state |a>, which is an eigenstate of $\mathbf{H_0}$ with energy E_a, and that there is a single photon present. We then calculate the probability of a transition induced by the interaction Hamiltonian **H'** to a state |b> with photon $\underline{k}'\lambda'$. For elastic scattering |b> = |a>. The transition probability per unit time can be calculated by the golden rule to second order perturbation theory. The fact that we have to go to second order perturbation theory for terms linear in $\underline{\mathbf{A}}$ immediately implies that besides the so-called non-resonant magnetic x-ray scattering, resonance phenomena will appear due to the energy denominator found in second order perturbation theory (compare the Breit-Wigner-formula for resonant scattering of the neutron from a nucleus). Here we will just quote the final result of this calculation: at moderately high x-ray energies and far away from all absorption edges of the elements in the sample, the elastic cross-section for scattering of photons with incident polarisation ε into a state of final polarisation ε' can written as:

$$\left.\frac{d\sigma}{d\Omega}\right|_{\varepsilon\to\varepsilon'} = \left[\frac{e^2}{mc^2}\right]^2 \cdot \left| \langle f_C \rangle_{\varepsilon'\varepsilon} + i\frac{\lambda_C}{d}\langle f_M \rangle_{\varepsilon'\varepsilon} \right|^2 \qquad (4)$$

Here $r_e = e^2/mc^2$ = 2.818 fm denotes the classical electron radius, λ_C = h/mc = 2.426 pm the Compton length of an electron. The scattering amplitudes $\langle f_C \rangle$ and $\langle f_M \rangle$ are given as matrices which describe the polarisation dependencies of charge and magnetic scattering, respectively. Here we discuss the case of linear polarisation, described by unit vectors perpendicular to the wave vectors of incident and scattered photons, $\underline{k}$ and $\underline{k}'$. σ-polarisation corresponds to the basis vector perpendicular to the scattering plane, π-polarisation corresponds to the vectors in the $\underline{k}$, $\underline{k}'$ plane. The basis vectors for the components of the magnetic moment of the sample and for the polarisation states are defined as follows, see figure 1:

$$\begin{aligned}
&\underline{\hat{u}}_1 = (\underline{k} + \underline{k}')/|\underline{k} + \underline{k}'| \\
&\underline{\hat{u}}_2 = (\underline{k}' \times \underline{k})/|\underline{k}' \times \underline{k}| \equiv \underline{\sigma} \equiv \underline{\sigma}' \\
&\underline{\hat{u}}_3 = (\underline{k}' - \underline{k})/|\underline{k}' - \underline{k}| = \underline{Q}/Q \\
&\underline{\pi} = \underline{\hat{k}} \times \underline{\sigma} \quad ; \quad \underline{\pi}' = \underline{\hat{k}}' \times \underline{\sigma}'
\end{aligned} \qquad (5)$$

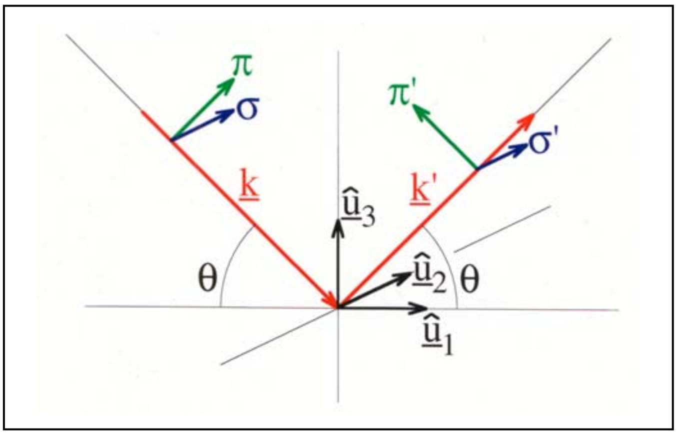

Fig. 1: *Illustration of the definition of the co-ordinate system and the basis vectors used to describe the polarisation dependence of x-ray scattering.*

In this basis the matrices in (4) can be written as

- <f_M> for the magnetic part:

$$\begin{array}{c|cc} \text{to}\backslash^{\text{from}} & \sigma & \pi \\ \hline \sigma' & S_2\cdot\cos\theta & \left[(L_1+S_1)\cdot\cos\theta+S_3\cdot\sin\theta\right]\cdot\sin\theta \\ \pi' & \left[-(L_1+S_1)\cdot\cos\theta+S_3\cdot\sin\theta\right]\cdot\sin\theta & \left[2L_2\cdot\sin^2\theta+S_2\right]\cdot\cos\theta \end{array} \tag{6}$$

- <f_C> for charge scattering:

$$\begin{array}{c|cc} \text{to}\backslash^{\text{from}} & \sigma & \pi \\ \hline \sigma' & \rho(\underline{Q}) & 0 \\ \pi' & 0 & \rho(\underline{Q})(\cos 2\theta) \end{array} \tag{7}$$

Here $S_i = S_i(\underline{Q})$ and $L_i = L_i(\underline{Q})$ (i=1, 2, 3) denote the components of the Fourier transform of the magnetisation density due to the spin and orbital angular momentum, respectively. $\rho(\underline{Q})$ denotes the Fourier transform of the electronic charge density distribution.

As can be seen from (4), magnetic scattering is a relativistic correction to charge scattering. For coherent elastic Bragg scattering, the ratio between the magnetic and the charge amplitude is determined by the momentum transfer and therefore we have written the pre-factor for the magnetic amplitude in the cross-section (4) as λ_C/d which emphasises that for a given Bragg reflection the ratio between magnetic and charge scattering is virtually independent of photon energy, at least to within the approximations leading to (4).

(4) contains three terms: pure Thomson-scattering, purely magnetic scattering and an interference term. The latter becomes important if charge- and magnetic scattering occur at the same position in reciprocal space, which is the case for ferromagnets. Note, however, that the prefactor "i" in front of the magnetic scattering amplitude means that magnetic scattering is shifted in phase by $\pi/2$ as compared to charge scattering. Therefore if both amplitudes, <f_C> and <f_M> are real, the interference term vanishes. The interference can only be observed, if one of the amplitudes contains an imaginary part (e. g. non centrosymmetric structures or photon energy close to an absorption edge for charge scattering) or if circular polarised radia-

tion is used. The importance of the interference term for ferromagnets becomes evident, if we consider the ratio between magnetic and charge scattering amplitudes. An estimate for this ratio can be given as:

$$\frac{< f_M >}{< f_C >} \sim \frac{\lambda_C}{d} \cdot \frac{N_M f_M}{N \cdot f} \cdot \langle S \rangle \tag{8}$$

Here, $N(N_M)$ and $f(f_M)$ denote the number and the form factor of all (the magnetic) electrons, $\langle S \rangle$ the expectation value of the spin quantum number. Using appropriate values for the parameters in (8), one finds that the amplitude for magnetic scattering is typically three orders of magnitude smaller than the amplitude of charge scattering, resulting in an intensity ratio of 10^{-6} between pure magnetic and pure charge scattering. It is not practical to measure a 10^{-6} effect in intensities. Therefore for ferromagnets, where charge and magnetic scattering coincide in reciprocal space, the interference term between charge and magnetic scattering is the leading term after charge scattering. In a very similar way to flipping-ratio measurements in neutron scattering, the direction of the magnetisation (or the incident photon polarisation) is changed periodically to change the sign of the interference term and thus extract this term from the pure charge scattering.

(6) and (7) show that magnetic scattering can be discriminated from charge scattering by a polarisation analysis experiment, where the off-diagonal terms $\sigma \rightarrow \pi'$ or $\pi \rightarrow \sigma'$ are being measured. Finally, (6) shows that the spin and orbital contributions have different angular- and polarisation dependencies and can therefore be distinguished in principle.

We have sketched a derivation of the non-resonant magnetic scattering cross sections starting from non-relativistic quantum mechanics and applying perturbation theory up to second order. It should be noted that the scattering cross-section can also be derived in a purely classical theory [10]. It turns out that the classical calculation reproduces the quantum mechanical cross-section for the spin part, but not for the orbital part. De Bergevin and Brunel [3] have drawn a simple diagram, representing the various interaction processes in such a classical model. This diagram is reproduced as figure 2.

The first process shown in figure 2 is the classical charge or Thompson scattering: an electromagnetic wave is incident on a free electron and due to the Coulomb force between the electric field vector and the charge of the electron, the electron is accelerated into a harmonic oscillation and re-radiates electric dipole radiation. The three other processes only appear if the electron carries a spin momentum, i. e. these processes give rise to magnetic x-ray scattering. The second process in figure 2 arises from the same Coulomb interaction with the incident electromagnetic wave. The accelerated spin moment gives rise to re-radiation of magnetic quadrupole radiation. In the third and fourth process of figure 2, the interaction with the incident electromagnetic field is between the spin moment and the magnetic field vector.

From figure 2, the polarisation dependence of charge and magnetic scattering becomes immediately evident. In charge scattering, the polarisation of the incident wave is conserved. From our simple classical pictures, it is immediately evident that the matrix (7) has to be diagonal. The cos 2θ factor for $\pi \rightarrow \pi'$-scattering is simply explained by the projection of the acceleration vector onto a plane perpendicular to the observation direction. Figure 2 shows that in contrast to charge scattering, the polarisation can indeed change for magnetic x-ray scattering. Therefore the existence of off-diagonal terms in the matrix (6) can easily be motivated from the classical picture figure 2. Polarisation analysis allows us to clearly distinguish charge and magnetic scattering.

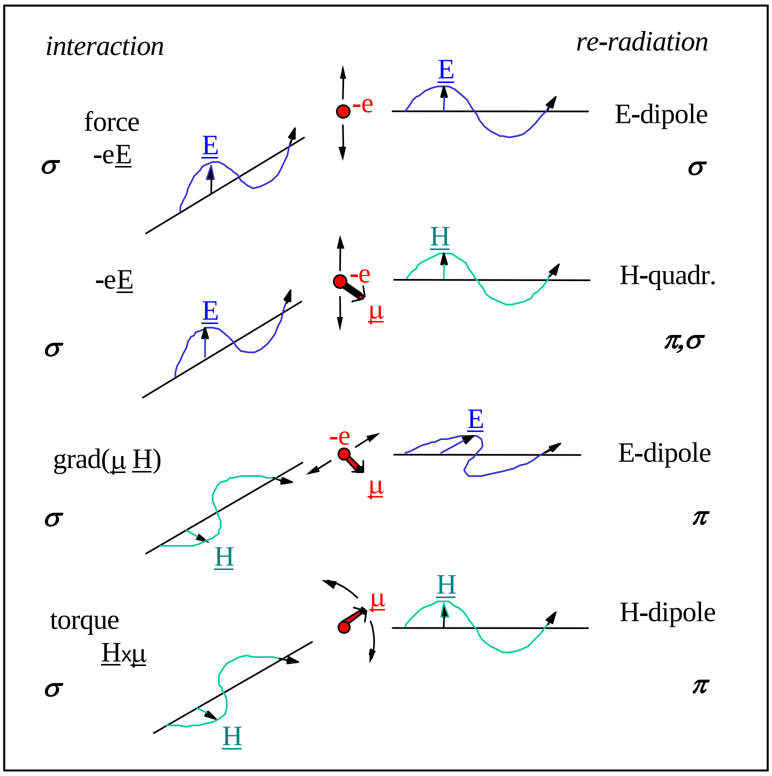

Fig. 2: *Illustration of the processes leading to scattering of x-rays by the charge (top) and the spin moment (bottom three) of the electron in a classical picture (from [3]).*

For what follows it is of interest to examine the high energy limit of the purely magnetic diffraction cross section. It can be easily calculated from (6). In this limit, the cross-section becomes virtually independent of polarisation and is sensitive only to the component of the Fourier transform of the spin density distribution perpendicular to the scattering plane:

$$\left.\frac{d\sigma}{d\Omega}\right|_{magnetic} = r_0^2\left(\frac{\lambda_C}{d}\right)^2 \left|S_2(\underline{Q})\right|^2 \tag{9}$$

Thus at high photon energies around 100 keV, the pure spin density distribution becomes accessible without polarisation analysis, while in neutron diffraction always the sum L+2S is being measured.

If the x-ray energy is tuned to the absorption edge of magnetic elements, resonance phenomena occur due to second order perturbation theory [11]:

$$\frac{d\sigma}{d\Omega} \sim \sum_c \frac{<a|\mathbf{O}^+(\underline{k}')|c><c|\mathbf{O}(\underline{k})|a>}{E_a - E_c + \hbar\omega - i\Gamma/2} \tag{10}$$

Here |c> denotes an intermediate excited state with energy E_c, $\hbar\omega$ the photon energy and Γ the level width of the excited state due to the finite lifetime $(\Gamma \cdot \tau \approx \hbar)$. The operator $\mathbf{O}(\underline{k})$ is given by the expression:

$$\underline{\mathbf{O}}(\underline{k}) = \sum_i e^{i\underline{k}\cdot\mathbf{r}_i}\left(\underline{\mathbf{P}}_i - i\hbar(\underline{k}\times\underline{\mathbf{s}}_i)\right) \tag{11}$$

(10) gives rise to anomalous dispersion, i. e. an energy dependence of the charge scattering, as well as to resonant magnetic scattering. The operator (11) can be expanded in a multipole series. It turns out that in the x-ray regime, the spin and orbital contributions can be neglected in most cases, and only the electric multipole terms have to be retained. These electric multipole

(predominantly dipole and quadrupole) operators induce virtual transitions between core levels and unoccupied states above the Fermi energy with subsequent reemission of a photon. These processes become sensitive to the magnetic state in exchange split bands due to the difference in occupation of minority and majority bands leading to so called resonance exchange scattering XRES [12] as illustrated schematically in figure 3.

Due to the resonance denominator in (10), resonance enhancements occur at the absorption edges of the magnetic elements. The strengths of these enhancements for XRES depend mainly on three factors:

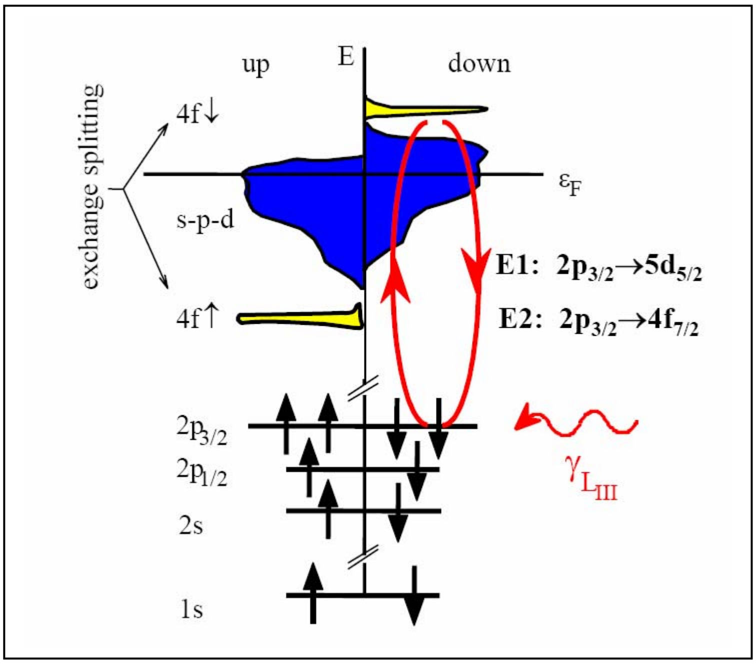

Fig. 3: *Schematic illustration of the second order perturbation process leading to XRES in the case of a lanthanide metal, e. g. a* Gd^{3+} *- ion.*

1. The magnitude of the transition matrix element. Dipole transitions between states |a> and |c> differing in orbital angular momentum quantum number by $\Delta L = 1$ are generally stronger than quadrupolar transitions with $\Delta L = 2$. A large overlap of the wave functions |a> and |c> favours large transition matrix elements. In contrast, transitions from "s" core levels to "p" or "d" excited states do not show large resonance enhancements due to the small overlap of the wave functions.
2. The difference in the density of empty states above the Fermi level for minority and majority spin states. To give an example: in lanthanide metals, the 5d bands are spin polarised due to the magnetic 4f states. However, the exchange splitting in the 5d is much weaker as compared to the 4f states and dipolar transitions 2p → 5d are sometimes not much stronger than quadrupolar transitions 2p → 4f.
3. The strength of the spin-orbit coupling in the ground- and excited states. Only due to this coupling do the electric multipole transitions become sensitive to the spin magnetism.

Using these criteria, we can qualitatively categorise the possible transitions according to the magnitude of the resonance enhancement, see Tab. 1. Here we define the term "resonance enhancement" as the ratio between the intensity of magnetic Bragg peaks in the maximum of the resonance relative to the intensity for non-resonant magnetic scattering.

elements	**edge**	**transition**	**energy range [keV]**	**resonance strength**	**comment**
3d	K	$1s \rightarrow 4p$	5 - 9	weak	small overlap
3d	L_I	$2s \rightarrow 3d$	0.5 - 1.2	weak	small overlap
3d	L_{II}, L_{III}	$2p \rightarrow 3d$	0.4 - 1.0	strong	dipolar, large overlap, high spin polarisation of 3d
4f	K	$1s \rightarrow 5p$	40 - 63	weak	small overlap
4f	L_I	$2s \rightarrow 5d$	6.5 - 11	weak	small overlap
4f	L_{II}, L_{III}	$2p \rightarrow 5d$ $2p \rightarrow 4f$	6 - 10	medium	dipolar quadrupolar
4f	M_I	$3s \rightarrow 5p$	1.4 - 2.5	weak	small overlap
4f	M_{II}, M_{III}	$3p \rightarrow 5d$ $3p \rightarrow 4f$	1.3 - 2.2	medium to strong	dipolar quadrupolar
4f	M_{IV}, M_V	$3d \rightarrow 4f$	0.9 - 1.6	strong	dipolar, large overlap, high spin polarisation of 4f
5f	M_{IV}, M_{II}	$3d \rightarrow 5f$	3.3 - 3.9	strong	dipolar, large overlap, high spin polarisation of 5f

Tab. 1: *Magnitude of the resonance enhancements for XRES for some elements relevant for magnetism. Only order of magnitude estimates are given with "weak" corresponding to a factor of about "10^0", "medium" to about "10^2" and "strong" to "$>10^3$".*

Tab. 1 only lists some of the most prominent examples. It demonstrates that the resonance enhancements for 3d transition metal ions is negligible in the hard x-ray regime (e. g. [13]), while it can be strong for soft x-rays. Unfortunately, at wavelengths of 12 to 30 Å, atomic resolution cannot be obtained under normal conditions. However, the transition metal L_{II} and L_{III} edges turn out to be extremely important for the investigation of magnetic thin films and nanostructures (e. g. [14]). For the 4f elements, resonance enhancements of about two orders of magnitude are observed in the hard x-ray range at the L_{II} and L_{III} edges (e. g. [15]). At these edges, dipolar transitions are in general dominant, but quadrupolar transitions can be significant. The so-called "branching ratio", i. e. the ratio between resonance enhancement at the L_{II} edge and the L_{III} edge has a tendency for a systematic variation along the rare earth series. While it is close to 1 for rare earth ions with seven 4f electrons, the L_{III} resonance is generally stronger for ions with more than seven 4f electrons while the L_{II} resonance tends to be stronger for less than half filling of the 4f shell. As in the case of the 3d transition metals, the soft x-ray range with the M_{IV} and M_V resonances is of importance for magnetic nanostructures [16]. At the M_{IV} edge of actinides, the intensity gain due to XRES can be as high as seven orders of magnitude [17]. Finally, we have not listed the 4d and 5d transition metal elements in Tab. 1, even so resonance enhancements at the L_{II} and L_{III} edges can be so large that surface magnetic x-ray diffraction becomes possible, e. g. in Co_3Pt (111) $(L_{III}^{Pt} \approx 11.5\,\mathrm{keV} : 2p_{3/2} \rightarrow 5d)$ [18]. We can conclude that XRES can provide large intensity gains for magnetic x-ray scattering, allows a spectroscopy of the exchange split empty states above the Fermi level and renders magnetic diffraction sensitive to the magnetic species.

Let us come back to the explicit form of the cross-section, including resonant magnetic scattering. We start from (10), which gives the general form of the cross-section for anomalous scattering. In what follows, we will neglect the spin dependent part and limit ourselves to electric dipole transitions. Detailed derivations are given in [11], [12] and the polarisation dependence, also for the case of electric quadrupole transitions, is discussed in [19]. Anomalous scattering becomes relevant close to the absorption edges of the elements. Then, an energy dependent amplitude has to be added to the expression (4) for the scattering cross-section. In dipole approximation, this amplitude reads:

$$f_{res}^{E1}(E) = f_o(E) + f_{circ}(E) + f_{lin}(E) \tag{12}$$

with

$$\begin{aligned} f_0(E) &= (\underline{\varepsilon}'\cdot\underline{\varepsilon})\ [F_{+1}^1 + F_{-1}^1] \\ f_{circ}(E) &= i(\underline{\varepsilon}'\times\underline{\varepsilon})\cdot m\ [F_{-1}^1 - F_{+1}^1] \\ f_{lin}(E) &= (\underline{\varepsilon}'\cdot\underline{m})(\underline{\varepsilon}\cdot\underline{m})[2F_0^1 - F_{+1}^1 - F_{-1}^1] \end{aligned} \tag{13}$$

f_0 is independent of the magnetic state (i. e. the conventional anomalous charge scattering), while f_{circ} and f_{lin} are the amplitudes connected for the special case of forward scattering with circular and linear dichroism, respectively. All three amplitudes have different polarisation properties. f_{circ} depends linear on the magnetic moment $\underline{m}$, while f_{lin} depends quadratic on $\underline{m}$. Therefore for antiferromagnets, only f_{circ} gives a contribution at positions in reciprocal space separated from the main charge reflections by the magnetic propagation vector. Finally, for a simple excitation into one atomic-like level, the energy dependence of the amplitudes is contained in the oscillator strengths

$$F_M^1 = \frac{\alpha_M}{(\omega - \omega_{res}) - i\,\Gamma/2\hbar} \tag{14}$$

Here ω denotes the photon energy, ω_{res} the position of the absorption edge and Γ the resonance width. The phenomenological parameter α_M gives a measure for the amplitude of the resonance and stands for the product of the transition matrix elements.

After this discussion of the cross section for non-resonant magnetic x-ray diffraction and for resonance exchange scattering, we will now demonstrate the possibilities of these techniques by some illustrative examples. Just for convenience most of these examples are from our own research, while we are very well aware of the beautiful work done by other groups. However, before presenting these examples, we have to discuss the experimental conditions for observation of magnetic x-ray scattering.

3 Experimental consideration

Figure 4 shows the sketch of a synchrotron x-ray source, indicating the special properties of the radiation.

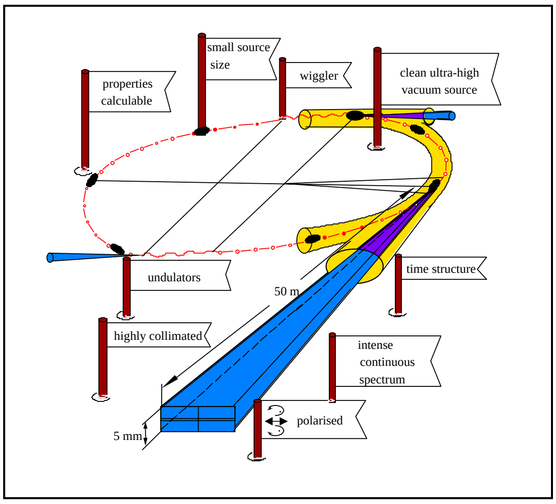

Fig. 4: *Schematic sketch of a synchrotron x-ray source.*

In a synchrotron x-ray source, electrons or positrons are circulating in bunches in a vacuum chamber at a velocity close to the speed of light. They are kept in the curved storage ring by magnetic fields that accelerate the charged particles with the Lorentz-force in a direction transverse to their propagation direction. The radially accelerated particles emit electromagnetic radiation. Due to their relativistic movement, this radiation is very much collimated in forward direction with an opening angle $\theta \approx 2/\gamma$, where $\gamma = E/m_0c^2$ with E = particle energy, $m_0c^2 \approx 511$ keV = energy equivalent of the rest mass of an electron. This is a consequence of the so-called relativistic Doppler effect, which results from the transformation of the emitted electromagnetic field distribution from the moving eigenframe of the charged particles into the laboratory system. The high collimation of the beam is essential for the observation of magnetic scattering, since one can conduct the experiment in such a way that only the desired scattering channel is excited, which leads to a significant better peak-to-background ratio as compared to conventional x-ray tubes. Moreover, the beam is highly polarised with a linear component in the orbital plane of the storage ring and elliptical polarisation of opposite sense above and below the orbital plane. Again, this polarisation of the beam is essential for magnetic scattering, since it allows one to separate experimentally charge-, spin- and orbital contributions to the scattered intensity, see chapter 2. Synchrotron radiation exhibits a continuous "white spectrum". This property makes possible investigations, where the x-ray energy has to be tuned to the absorption edge of an element in the compound under investigation. While at x-ray tubes intense radiation is emitted only for the characteristic lines of the anode material, one can choose a narrow energy band width of the synchrotron radiation, just by applying a grating (for soft x-rays) or crystal-Bragg (for hard x-rays) monochromator. Modern synchrotron radiation sources do not just use the radiation of the so-called bending magnets, but mainly employ insertion devices, such as wigglers and undulators as even more powerful radiation sources. Both types of insertion devices are permanent magnet structures, which create an alternating field, perpendicular to the orbital plane of the storage ring. This field leads to a sinusoidal movement of the charged particles within the insertion devices. At each reversal point, radiation is emitted similar to the radiation from the dipolar magnets. The difference between wigglers and undulators lies in the amplitude of the sinusoidal movement. This amplitude is large for wigglers, giving rise to an incoherent superposition of the radiation from the various magnet poles. Therefore, the wiggler spectrum resembles the spectrum of a bending magnet, but the intensity is amplified by a factor corresponding to the number of magnet poles. In an undulator, where the amplitude of the sinusoidal movement is smaller, the radiation from the various poles superimposes coherently in forward direction. This leads to a line-spectrum in energy with odd harmonics on axis. The intensity within these lines is proportional to the square of the number of magnet poles in the undulator. The position of the undulator harmonics can be tuned by the strength of the magnetic field or the undulator period. In practical devices, the magnetic structure is realised by permanent magnets and the magnetic field strength can be varied by opening or closing the undulator gap. In an undulator, coherence is achieved for the following condition:

$$\lambda = \frac{\lambda_u}{2\gamma^2}\left(1 + \frac{K^2}{2} + \gamma^2\theta_0^2\right) \tag{15}$$

Here λ_u denotes the undulator period, γ the particle beam energy, expressed in units of the energy equivalent of the electron restmass $m_ec^2 \approx 511$ keV, θ_0 is the angle of emittance and K the so-called wiggler or undulator parameter

$$K = \frac{\lambda_u eB}{2\pi m_e c} = \gamma \cdot \theta_w \tag{16}$$

Here, B is the amplitude of the magnetic field on axis and θ_w the maximal angle of deviation of the particle against the nominal orbit. In figure 5, the spectra of bending magnet, wiggler and undulator are compared. Since the undulator radiation is quasi-monochromatic with a energy width inverse proportional to the number of magnetic poles and has a high collimation with an opening angle of $2/\gamma$ (about 0.1 mrad for a 5 GeV machine) in both directions, undulator radiation resembles already very much a laser beam known from optics. Its unique properties make the undulator the x-ray source of the choice for magnetic x-ray scattering applications.

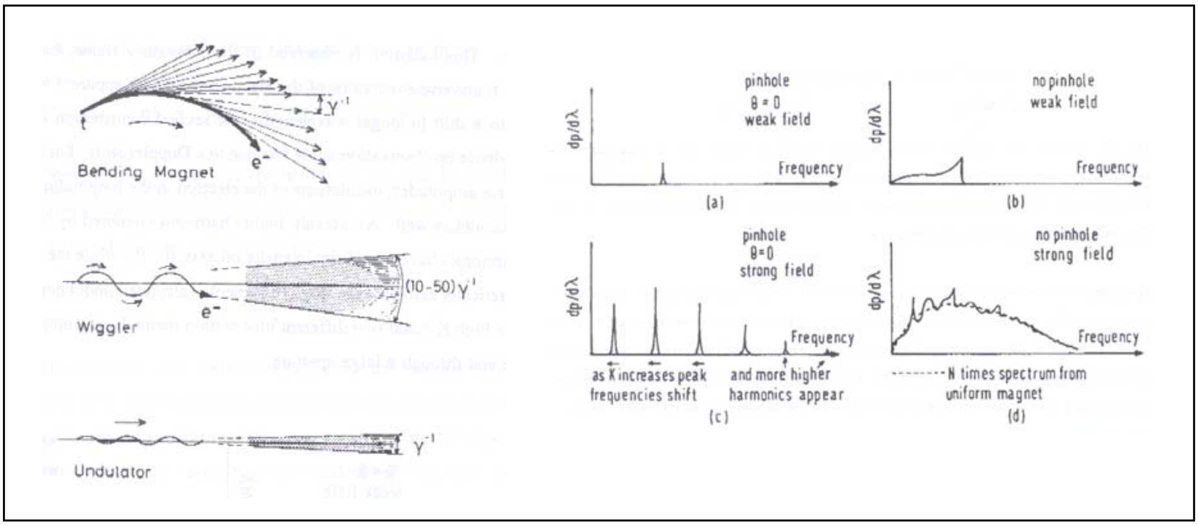

Fig. 5: *left: comparison of the emittance characteristics for a bending magnet, a wiggler and an undulator. right: Frequency spectrum of undulator radiation. The dashed line in d corresponds to a wiggler spectrum. (from Saile, 23. IFF-Ferienkurs 1992)*

Worldwide, there exist three so-called "third generation synchrotron sources" for the hard x-ray regime: the *European Synchrotron Radiation Facility ESRF* in Grenoble, *SPRING-8* in Japan and the *Advanced Photon Source (APS)* in Argonne, USA. All three facilities have storage rings with a circumference of about 1 km and feature beamlines dedicated to magnetic scattering. The typical set-up of such a beamline is as follows: the beam from an undulator source is tailored by slit systems. Mirrors are used to suppress higher harmonics in the x-ray beam and/or to focus the beam onto the sample in the experimental hutch. The x-ray energy is selected by a double crystal Bragg monochromator. To handle the high heatload of several hundred W/mm^2, liquid nitrogen cooled silicon crystals are employed for monochromatisation. Usually the 111 reflection is chosen, since the second harmonic is largely suppressed for the Si crystal structure by the diamond glide planes. This beamline optics is situated in a so-called optics hutch with lead walls serving as biological radiation shielding. In the optics hutch, the x-ray beam is prepared with a desired properties and then enters the experimental hutch, where the actual scattering experiment is situated. The polarisation of the incident beam is monitored with two orthogonal scintillation detectors, which use the emittance characteristic of charge scattering, according to (7). The incident photon flux is being monitored with ionisation chambers. The sample is situated in the center of an Eulerian cradle, which allows arbitrary orientation of the sample in space. On the detector arm, an analyser unit is mounted, which serves to suppress background, enhance the resolution in reciprocal space, but also allows an analysis of the polarisation of the scattered beam. Such a polarisation analyser is shown in some more detail in figure 6.

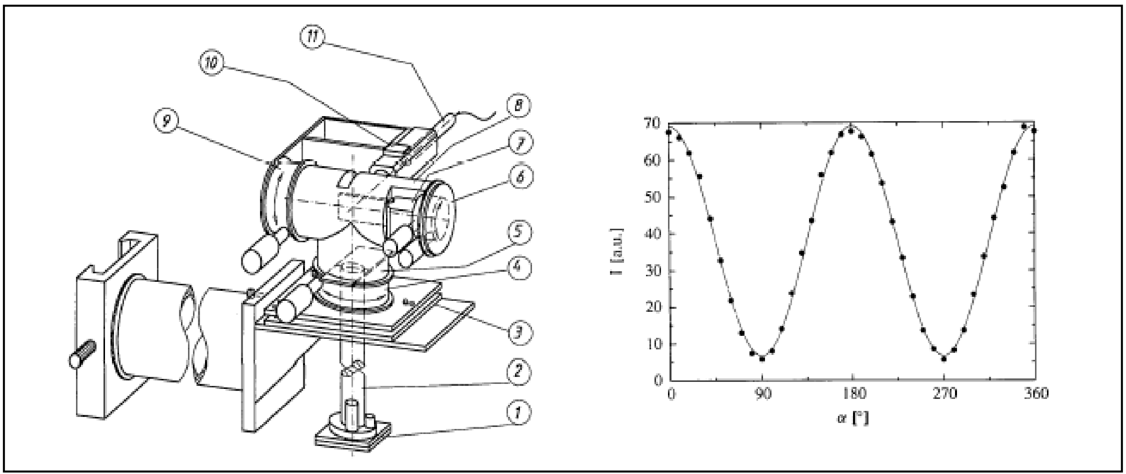

Fig. 6: *Polarisation analyser according to [37] and measurement of the polarisation of a wiggler beam.* ***1****: motorized double slit system;* ***2****: evacuated flight tube;* ***3****: base plate with three manual degrees of freedom for alignment;* ***4****: goniometer for the* α *movement (see text);* ***5****: entrance slit;* ***6****: goniometer for the* ω *movement of the analyser crystal;* ***7****: tilt of the analyser crystal;* ***8****: aluminium housing of the analyser;* ***9****: goniometer for the analyser* 2θ *movement;* ***10****: detector aperture slits;* ***11****: NaI detector.*

To analyse the polarisation of the scattered beam, one has to find a crystal with a reflection at a lattice d-spacing corresponding to 1/2 of the wavelength of the radiation d = $\lambda / 2$, allowing for 90° charge reflection. At $2\theta_A$ = 90°, the formfactor and the Debye-Waller-factor strongly reduce the reflected intensity. Therefore, the analyser crystal should have a very high peak reflectivity. On the other hand, it should accept the whole divergence of the beam, diffracted from the sample. Therefore, the best choice is a mosaic crystal, which compromises between high peak reflectivity and a sufficient width of the rocking curve. Often, pyrolytic graphite (PG002 and higher harmonics) is chosen as analyser, which, however, gives only very limited choice of wavelengths. Under the conditions of 90° charge scattering, only $\sigma \rightarrow \sigma$ scattering occurs. By rotating, the analyser crystal and detector around the beam axis (α-movement 4 in figure 6), the degree of polarisation of the x-ray beam can be determined. As an example, figure 6 shows the measurement of the polarisation of the monochromatic primary beam from a wiggler device at the DORIS storage ring in Hamburg. For an x-ray energy of 10.46 keV, a PG008 analyser crystal fulfills the 90° condition. The integrated intensities scattered from this analyser as a function of the angle α between the vertical and the scattering plane of the analyser, are being plotted together with a refinement according to

$$I(\alpha) = H\cos^2(\alpha - \alpha_0) + V\sin^2(\alpha - \alpha_0) \qquad (17)$$

Here, H and V denote the intensities corresponding to horizontal and vertical polarisation, respectively. α_0 describes the possible tilt. The degree of horizontal polarisation is given by

$$P = (H - V)/(H + V) \qquad (18)$$

In the case of this second generation synchrotron radiation source and for complete open entrance slit, a polarisation P of about 84 (1 %) was determined. Undulator radiation from modern 3^{rd} generation storage ring sources can have a degree of linear polarisation in the orbital plane above 99.5 %. At these modern beamlines, the incident flux can exceed 10^{13} photons/mm^{2}s.

According to (6), polarisation analysis in $\sigma \rightarrow \pi$ geometry is the most efficient way to distinguish between magnetic and charge scattering and thus also to suppress possible background from the sample. If no polarisation analyser is employed, background from Compton scattering or sample fluorescence has to be suppressed to enhance the peak-to-background ratio. A very efficient way to do this is by employing energy dispersive solid state detectors. They allow one to set an electronic window for the spectro-amplifier and thus to discriminate the elastic scattered photons from the background of inelastic scattering.

4 Resonance exchange scattering

As an example of the effect of resonance exchange scattering, we show in figure 7 raw data taken at the W1 beam line at HASYLAB for the L_{II} resonance of GdS [15]. Due to the high absorption cross section of Gd for thermal neutrons, no detailed neutron diffraction studies exist for GdS. With x-rays a comfortable count rate of about 3000 photons per second was obtained for the 9/2 1/2 1/2 reflection on resonance and we could verify the assumed type II antiferromagnetic ordering on the fcc lattice. While resonant exchange scattering can in principle give information about the density of unoccupied states above the Fermi level, most resonance line shapes can well be approximated with the simple two level model of equation (14). This is also true for the resonance shown in figure 7, where only a small asymmetry remains after absorption correction [15]. There are, however, examples of much more structured resonances with double and multiple peaks as a function of energy. Examples are the K-edge resonance of manganese in the perovskite type compound $RbMnF_3$ [13] or the L-edge resonances in the rare-earth metal Tb [28].

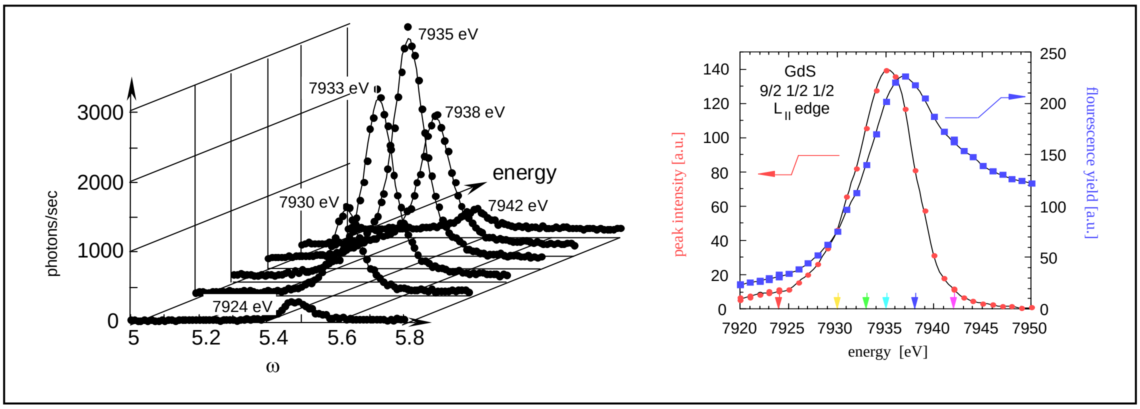

Fig. 7: *The resonance enhancement of the magnetic signal of the 9/2 1/2 1/2 superstructure peak of GdS at the Gd* L_{II} *edge measured at 4.2 K. The left diagram shows raw data of rocking curve scans at various photon energies. The right diagram shows as a function of photon energy the peak intensities together with the structure of the absorption edge.*

The strength of resonance exchange scattering that makes it unique compared to all other techniques is that it combines spatial resolution (in reciprocal Fourier space) with element specificity. By choosing a resonance, where an enhancement of several orders of magnitude for a specific magnetic element is obtained, non-resonant scattering becomes negligible and only the magnetic pair correlation functions for this element in question are observed. This can be nicely demonstrated for the mixed crystal series $Gd_{1-x}Eu_xS$. While GdS is an antiferromagnetic metal, EuS is a ferromagnetic insulator. For some intermediate concentration, a metal-insulator transition occurs. Moreover, since the system exhibits competing magnetic interactions (ferromagnetic versus antiferromagnetic), frustration occurs, i. e. not all magnetic bonds can be satisfied simultaneously. Frustration combined with disorder typical for a stochastic occupancy of the rare earth site in the solid solution, leads to a spin glass phase without magnetic long range order separating the ferromagnetic from the antiferromagnetic phase. Some questions that can be tackled with XRES are: can we observe the frustration mechanism and what is the magnetic microstructure of the long range ordered and of the spin glass phase? The answer to these questions lies in the study of the magnetic correlations with element specificity [29, 30].

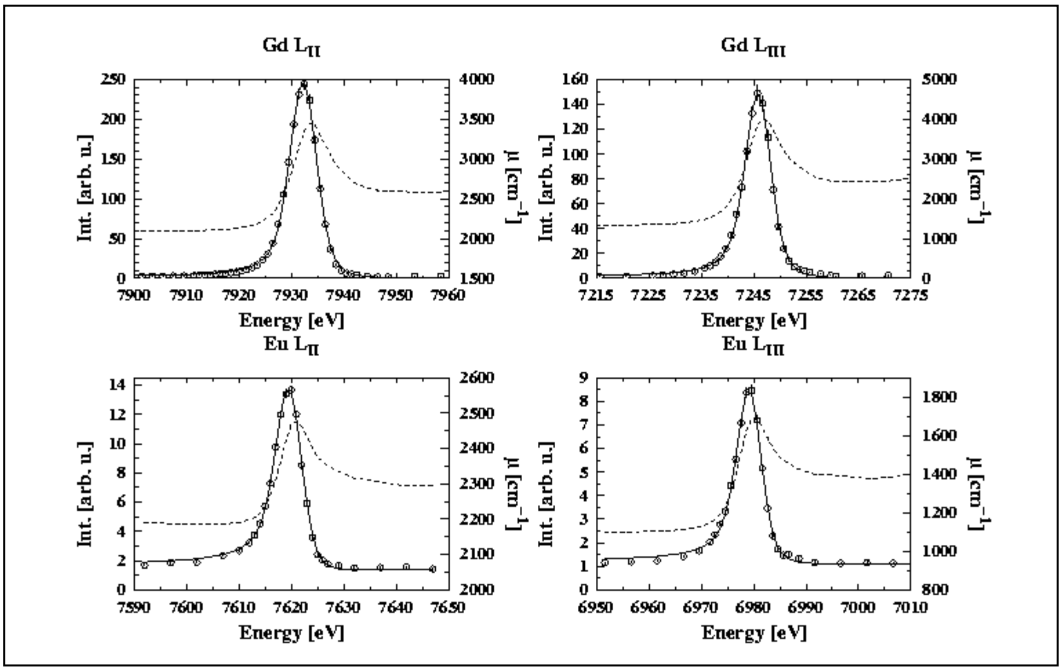

Fig. 8: *Absorption corrected energy dependence of the intensity of the* $^{1}/_{2}\ ^{1}/_{2}\ ^{9}/_{2}$ *magnetic Bragg reflection at the Eu and Gd* L_{II} *and* L_{III} *edges for a* $Gd_{0.8}Eu_{0.2}S$ *sample at 4 K. The solid line is a fit with (14), the dashed line shows the absorption coefficient.*

Figure 8 shows the resonance behaviour for a $Gd_{0.8}Eu_{0.2}S$ sample at all 4 L_{II} and L_{III} edges together with a fit assuming a simple atomic-like two level dipolar transition [29,30] (compare eq. (14)). The resonances for the two different elements are well separated in photon energy and the enhancement amounts to between one and more than two orders of magnitude compared to non-resonant scattering. This is the reason for the element specificity, as is illustrated in figure 9.

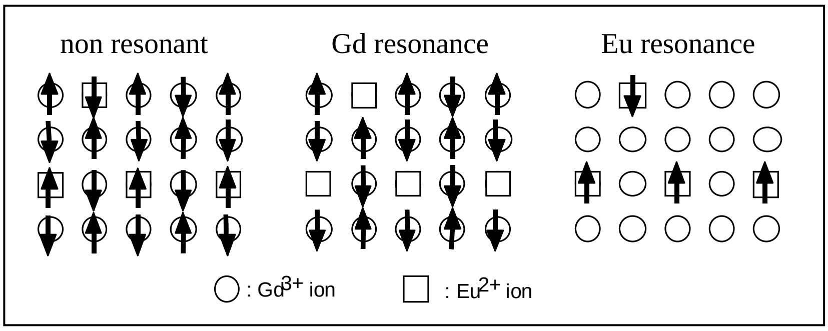

Fig. 9: *Illustration of the effect of XRES for* $Gd_xEu_{1-x}S$*: In the case of non-resonant x-ray diffraction or neutron scattering, the magnetic order is observed independent of the magnetic species. In the maximum of the resonance of Gd, only the ordering of the Gd moments is visible due to the large resonance enhancement. At the Eu resonances, only the order of the Eu moments is visible.*

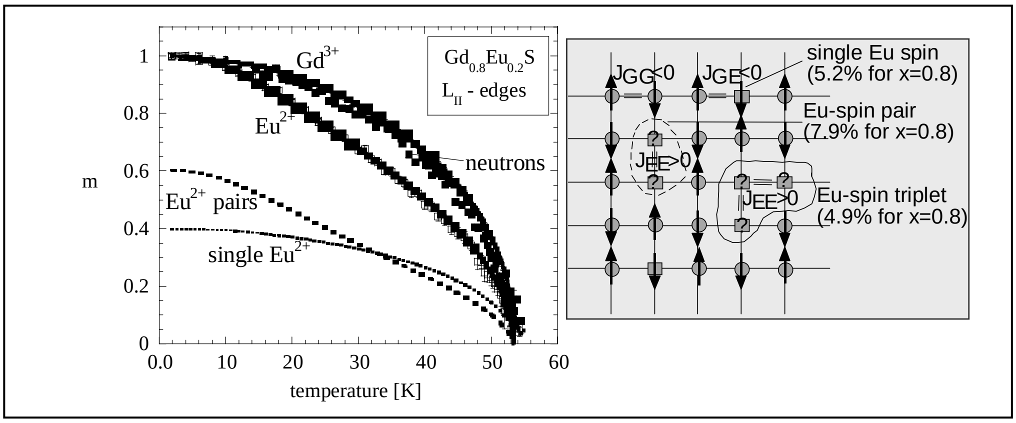

Fig. 10: *Temperature dependence of the element specific sublattice magnetisation for* $Gd_{0.8}Eu_{0.2}S$ *together with neutron data and a model refinement (left). The refinement is based on the frustration model illustrated on a 2d lattice on the right.*

Figure 10 shows the temperature dependence of the sublattice magnetisation determined with neutron diffraction (filled triangles), with XRES at the Gd L_{II} edge (small circles) and with XRES at the Eu L_{II} edge (open squares) [29, 30]. The sublattice magnetisation was obtained from rocking curves as the normalised square root of the integrated intensities. This is the correct procedure for the case of neutron diffraction. However, in the case of XRES, the intensity depends on transition matrix elements (compare (14)), which can, in principle, change with temperature. Scattering in second order perturbation theory is a priori not directly related to the order parameter. Therefore the neutron data were taken as a cross check: it turns out that the weighted sum of the XRES curves for Eu and Gd matches nicely the neutron curve, indicating that with XRES we measure indeed the sublattice magnetisation for each species Eu^{2+} and Gd^{3+} individually.

The surprising observation is that the sublattice magnetisation has a different temperature dependence for the two ions Eu^{2+} and Gd^{3+}, even so both have the same $^8S_{7/2}$ electronic ground state and they both are embedded “in the same sea of conduction electrons”. An explanation for this observation can be given, if we assume frustration effects to occur. In a very simple model, we start from an isotropic Heisenberg Hamiltonian

$$\mathbf{H} = -\sum J_{ij}\,\underline{\mathbf{S}}_{\mathbf{i}}\cdot\underline{\mathbf{S}}_{\mathbf{j}} \qquad (19)$$

with nearest neighbour interactions only, place the two ions at random on a simple cubic lattice and assume the exchange interaction between pairs of Gd-Gd and Gd-Eu to be antiferromagnetic and between pairs of Eu-Eu to be ferromagnetic. This will lead to frustration for pairs, triplets etc of Eu spins within the surrounding Gd matrix, see figure 10 (right). To calculate these frustration effects for the case of small Eu concentrations, we rewrite the Hamiltonian (19) in the form of a sum with one term for the Gd subsystem, including single Eu spins, and another term for the Eu “clusters” (pairs, triplets etc.). The size of the Eu “clusters” follows a binomial distribution. The Gd subsystem is treated in a mean field theory, while the Hamiltonian for the Eu pairs in the mean field of the surrounding Gd ions can be diagonalised exactly [29,30]. The result is shown in figure 10 (left): we obtain a surprisingly good agreement between theory and experiment, indicating that the abnormal temperature dependence of the Eu subsystem is actually due to frustration effects. With Monte Carlo simulations we can employ a more realistic interaction model with exchange up to second neighbours on the fcc lattice and obtain similar results. We observe a change from a collinear magnetic structure for GdS to a canted structure for the antiferromagnetic mixed crystals, see figure 11.

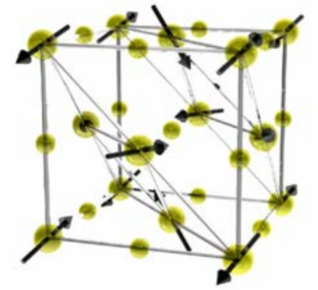

Fig. 11: *Antiferromagnetic structure of $Gd_{1-x}Eu_xS$ for small x as obtained from Monte Carlo simulations. While GdS has a collinear antiferromagnetic structure of type II on the fcc lattice (i. e. all spins on [111] planes are parallel and the magnetisations for neighbouring [111] planes are antiparallel), the doped crystals exhibit a canted spin arrangement.*

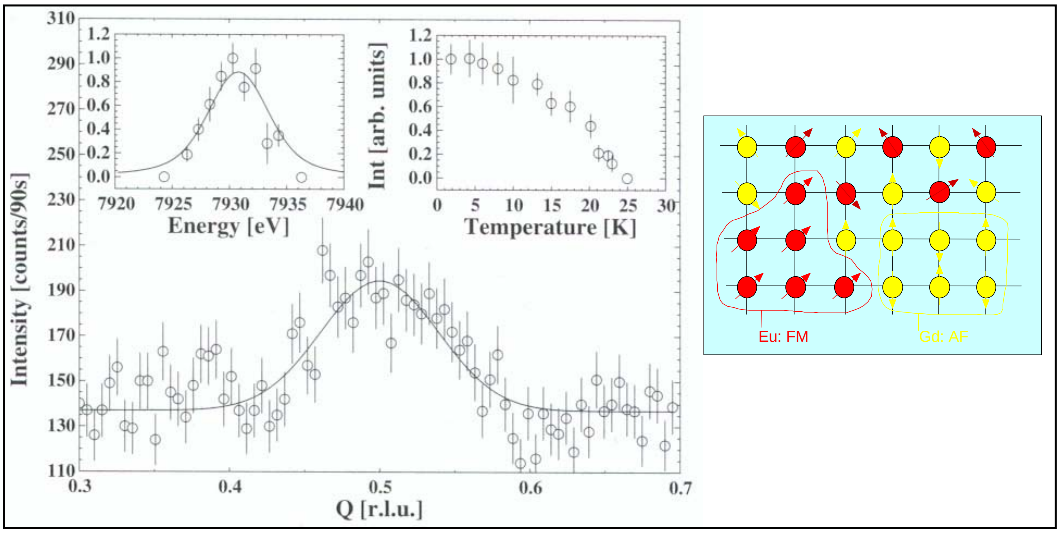

Fig. 12: *Linear scan in reciprocal space from (0.3 0.3 4.3) to (0.7 0.7 4.7) around the antiferromagnetic Bragg peak position for $Gd_{0.67}Eu_{0.33}S$ at a temperature of 4 K. The energy was tuned to the Gd L_{II} edge. A polarisation analyser with $\sigma \rightarrow \pi'$ geometry was used to suppress the background from charge scattering. The inserts show the energy and temperature dependencies. On the right a model for the spin glass state is shown.*

The combined occurrence of frustration and disorder can result in a spin glass phase for intermediate concentrations. In fact, we do not observe long range magnetic order for a x=0.33 sample. Instead, short range antiferromagnetic correlations are observed for the Gd subsystem with correlation lengths of about 40 Å, see figure 12. We could not detect any antiferromagnetic correlations at the Eu L_{II} or L_{III} edges. This leads us to the conclusion that a cluster spin glass state is formed for intermediate concentrations: while the Gd spins show antiferromagnetic correlations in regions of typical sizes of 40 Å, the Eu spins develop ferromagnetic correlations. These spin "clusters" freeze in into arbitrary directions, leading to the spin glass behaviour.

To conclude this section on $Gd_{1-x}Eu_xS$, we have shown which detailed information can be obtained with an element-specific probe: for this mixed crystal series we could reveal the frustration mechanism and verify that the spin glass state at intermediate compositions consists of a frozen cluster glass state. Such detailed information is not accessible with any other probe.

We can give one other example for the element specific information XRES offers. This example concerns thin film magnetism, namely Er/Tb rare earth super-lattices [31]. Such super-lattices, for which the single Er or Tb layers are just a few mono-layers thick, can be grown epitaxially with high quality on sapphire substrates. They show a rich magnetic phase diagram. Phase transition temperatures are altered compared to the bulk and some phases appear, which are not present in the bulk materials.

Here we want to discuss only one special feature for a multilayer consisting of 150 double layers of 20 mono-layers of Er and 5 mono-layers of Tb: $[Er_{20} / Tb_5]$ x 150. In a temperature range between 80 K and 130 K, magnetic satellite peaks appear, which indicate that a helical magnetic structure with a propagation vector close to the one for bulk Er is formed throughout the multilayer, despite the fact that the Tb layers show basal plane ferromagnetic order. The satellite peaks are resolution limited, which shows that the phase information for the magnetic helix is carried through the ferromagnetic Tb layers. Can XRES help us to understand the coupling mechanism of the Er layers through ferromagnetic Tb layers? Indeed it can: if we tune the x-ray energy to the L_{II} or L_{III} absorption edges of Tb, we enhance its magnetic scattering and can thus observe specifically what happens within the Tb layers. Figure 13 shows a plot of a XRES measurement as a function of x-ray energy and a reciprocal space co-ordinate. These data tell us that XRES peaks at an energy corresponding to the Tb L_{III} edge and at a Q-space position corresponding to the propagation vector of the Er magnetic helix.

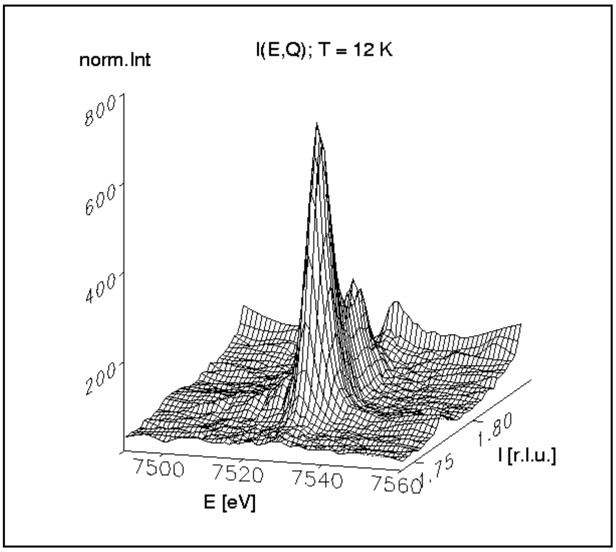

Fig. 13: *XRES from an $[Er_{20}/Tb_5]x150$ rare earth super lattice measured as a function of x-ray energy in linear Q-scans along the [000l] axis. The intensity peaks at an energy corresponding to the Tb L_{III} resonance energy and a Q-space position close to the magnetic propagation vector of bulk Er.*

However, from neutron scattering, we know that the 4f moments of Tb are aligned ferromagnetically. This apparent contradiction can be resolved, if we consider the XRES process depicted schematically in figure 3. Polarisation analysis tells us that the relevant transitions are dipolar in nature. Therefore, the intermediate states in the XRES process are the 5d conduction band states and with XRES, we do not observe the 4f magnetic order, but the spin polarisation of the 5d conduction electrons in the Tb layer. Apparently, these conduction band electrons form a spin density wave within the Tb layers corresponding to the helical magnetic order in the Er layers. They carry the phase information through the Tb interlayers and thus allow the Er layers to develop a coherent helical magnetic structure throughout the super lattice.

To conclude this section, we have shown that the information provided by XRES is not only element specific, but also specific to the electronic state of this element (4f versus 5d electrons). In the case of rare earth superlattices, XRES allows a direct observation of the interlayer coupling mechanism. Spin polarisation in the conduction band is observed, as predicted by the RKKY exchange mechanism.

So far, we have only discussed XRES from antiferromagnetic structures, for which magnetic and charge scattering are well separated in reciprocal space. Due to the high brilliance of the modern synchrotron radiation sources, even a small magnetic signal can be readily observed. Polarisation analysis helps to distinguish charge and magnetic scattering and allows to suppress the charge background.

For ferromagnetic samples, the situation is quite different. Here charge and magnetic scattering coincide. Since magnetic scattering is typically orders of magnitude weaker as compared to charge scattering, it becomes difficult to observe. Combining (4) and (12), the cross section for magnetic scattering takes the form:

$$\frac{d\sigma}{d\Omega} = |f|^2 = |f_C + f_R(E)|^2 \tag{20}$$

Here, f_C denotes the amplitude for charge scattering, f_R the amplitude for resonance exchange scattering, and we have neglected non-resonant magnetic scattering close to a relevant absorption edge. Let us now chose the scattering geometry depicted in figure 14.

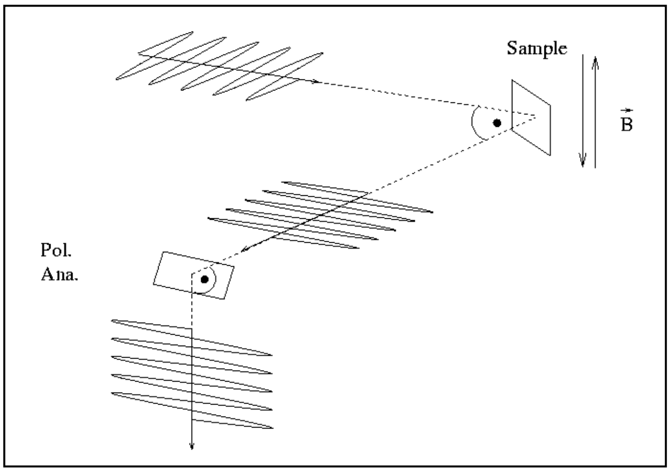

Fig. 14: *Experimental set-up for the measurement of XRES from ferromagnetic samples. The primary beam is polarised horizontally, the magnetic field is applied perpendicular to the horizontal scattering plane and a polarisation analyser is employed to suppress the vertically polarised component.*

In this geometry, $|f_{circ}|$ of eq. (13) is maximised, since in saturation $\underline{m} \parallel (\underline{\varepsilon}' \times \underline{\varepsilon})$. The resonant amplitude f_{circ} is proportional to the expectation value of the z-component of the magnetic moment $\langle m_z \rangle$. Then the form of the cross section (20) will lead to the following form of the ferromagnetic Bragg intensities:

$$I = I_{mag}\left\langle m_z^2\right\rangle + I_{\mathrm{int}}\left\langle m_z\right\rangle + I_{charge} \tag{21}$$

There are three contributions to the scattered intensity I: a pure charge term I_{charge}, a pure XRES term I_{mag} and an interference term between charge and XRES scattering I_{int}. By switching the direction of the external magnetic field, an asymmetry ratio

$$R_a \equiv \frac{I^{\uparrow} - I^{\downarrow}}{I^{\uparrow} + I^{\downarrow}} \tag{22}$$

can be measured.

In the case of EuS and with the scattering geometry of figure 14, this asymmetry ratio is as large as 67 % [32]. In fact, magnetic scattering, interference term and charge scattering become quite comparable in magnitude. Figure 15 shows the L_{II} resonance of EuS at 4 K.

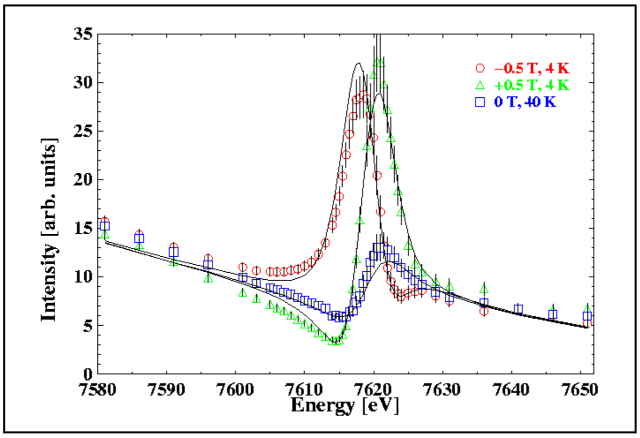

Fig. 15: *Absorption-corrected energy dependence of the (115) reflection measured at the Eu-L_{II} edge. Two measurements with magnetic fields of +0.5 T and –0.5 T were performed at 4 K and one measurement at 40K well above the Curie temperature of 17 K. The solid line represents a refinement, see text.*

Such data can be used to obtain spectroscopic information about the electronic states at the Fermi energy. In [32] a model has been refined to the data, which assumes that the empty states available for spin-up and spin down electrons are narrow, but shifted by an exchange energy ε. The value for this exchange splitting was determined to ε = 0.27(1) eV.

To conclude this section, we have shown that XRES can also be measured from ferromagnetic samples. This allows one to measure element specific hysteresis loops. Spectroscopic information about the intermediate states close to the Fermi energy can be obtained from the shape of the resonance curves. In order to determine values such as the exchange splitting unambiguously, it is however, not sufficient to just measure the asymmetry ratio (22). Instead, several data sets with the energy dependencies for positive and negative field and for pure charge scattering have to be refined.

5 Non-resonant magnetic x-ray diffraction

Resonant magnetic x-ray scattering has the convenience of easily detectable signals due to the resonance enhancement and provides element specific information. Therefore many magnetic x-ray diffraction studies nowadays deal with resonance exchange scattering. However, for transition metal ions, only K-edges lie in the range of hard x-ray wavelengths, where atomic resolution is achievable. Due to the dipolar and quadrupolar selection rules and the small overlap between core 1s-states and the magnetic sensitive 3d or 4p energy bands, resonance enhancements are negligible at transition metal K-edges and one is left with neutron- or non resonant magnetic x-ray scattering. These techniques have the advantage that they measure directly the order parameter, in contrast to resonant scattering, where transition matrix elements are involved, which are not known a priori. Moreover, the form of the cross section (6) suggests that spin $\underline{S}$ and orbital $\underline{L}$ angular momentum can be determined separately by means of polarisation analysis. Take the example of a collinear antiferromagnet for which charge – and magnetic reflections are well separated in reciprocal space and for which we can align the moments along the $\underline{\hat{u}}_2$ – axis, i.e. $\underline{S}(\underline{Q}) = (0,S(\underline{Q}),0)$ and $\underline{L}(\underline{Q}) = (0,L(\underline{Q}),0)$. At the antiferromagnetic reflections charge scattering vanishes and, according to (6), magnetic scattering only occurs in the $\sigma\rightarrow\sigma'$ and the $\pi\rightarrow\pi'$ polarisation channels. In the former, scattering is sensitive to $S(\underline{Q})$ only, in the latter, it is sensitive to a linear combination of $S(\underline{Q})$ and $L(\underline{Q})$, thus allowing a unique determination of the ratio between both contributions. While such a model independent separation of S and L cannot be achieved with neutron scattering due to the fact that the neutron cross section is proportional to L+2S, it provides very important information e.g. to verify band structure calculations. Such a separation of S and L by means of polarisation analysis of non-resonant magnetic x-ray diffraction has for example been done in Ho [5], NiO [20] or Cr [21].

When discussing non-resonant magnetic x-ray diffraction, one has to start with the beautiful pioneering work by Gibbs et al. [4] and Bohr et al. [34] on Ho metal. Together with the following work [35], this is one of the most comprehensive studies of magnetic x-ray scattering so far undertaken. The basic magnetic structures in the heavy rare-earth metals are known for quite a long time from the pioneering experiments by Koehler et al. The results are illustrated in figure 16.

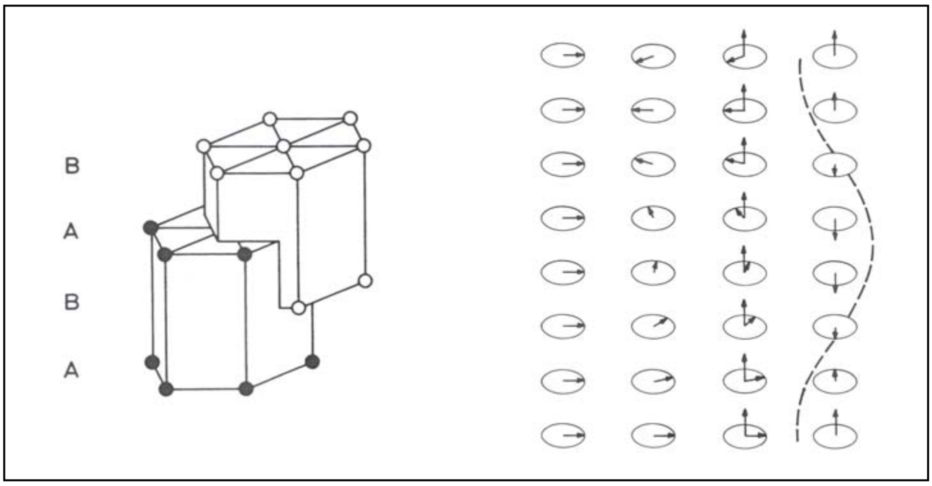

Fig. 16: *On the left, the hexagonal close packed hcp crystal structure realised in the heavy rare-earth metals is illustrated. On the right, the magnetic structures of the heavy rare-earth metals are sketched. From left to right: basal-plane ferromagnet, helix structure, cone structure and the c-axis modulated CAM structure.*

The moments in any particular hexagonal base-layer are parallel and only the relative alignment of different planes, when propagating along the hexagonal c-direction are illustrated. In Holmium, a helix structure is realised below the Néel temperature of 132 K down to 20 K, where a cone structure develops. In the high temperature region, the modulation period increases continuously with decreasing temperature, which indicates that the helix is incommensurate with the crystal lattice, i. e. the ratio between magnetic period and lattice period cannot be expressed as a simple rational number. At 20 K, a lock-in transition occurs and the magnetic modulation becomes commensurate with the chemical lattice with a period of 6 unit cells, i. e. 12 atomic layers, corresponding to $\tau = 1/6$. The beauty of the x-ray experiment was to show that much of what was originally thought to be an incommensurate phase in fact contains a series of subtle lock-in transitions. These details could be revealed because of the high wavevector resolution of 10^{-3} Å^{-1} for the synchrotron x-ray experiments. Subsequently, these observations have led to a new model of magnetism in Holmium and other rare-earth metals. In the experiments by Gibbs et al. the scattering vector $\underline{Q}$ was aligned parallel to the axis of the helical magnetic structure. In this case, we expect that the main charge peaks along $\underline{c}^*$ are accompanied by a pair of satellites at positions $\underline{Q}_{\text{helix}}=\underline{G}_n\pm\underline{\tau}$, where the turn angle from plane to plane of the helix is given by $\Phi = \tau \cdot d$. Figure 17 shows the original measurement by Gibbs et al. in the vicinity of the 0004 Bragg peak in Ho.

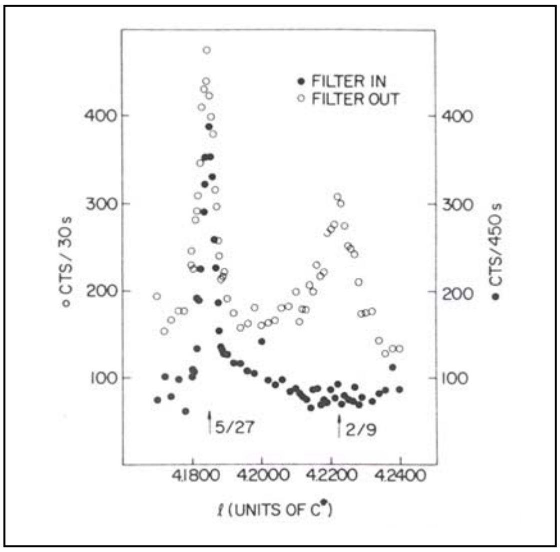

Fig. 17: *Scattering in the vicinity of the 0004 Bragg peak in Holmium at 17 K. The open circles show the scattering without polarisation analysis, while the filled circles show the scattering observed with a polarisation analyser aligned to observe only σ-π' scattering (from [4]).*

Without polarisation analysis two peaks are visible: one sharper satellite reflection and one, which is significantly broadened. Both reflections occur at rational positions indicating a commensurate structure. According to (6) and (7), magnetic scattering can be identified with the help of a polarisation analyser, aligned to observe the off-diagonal σ-π' scattering. This experiment is shown by the filled circles. Obviously, only the sharp peak is of magnetic origin, while the broader feature has to be assigned to charge scattering. For a pure spiral structure, no strain wave should occur due to magnetoelastic interactions. To resolve the puzzle, we can look at the temperature dependence of the magnetic modulation vector in holmium, deduced from x-ray and neutron data (see figure 18). With the high resolution x-ray data, several lock-in transitions as well as a hysteresis behaviour can be observed at low temperature. Figure 19 shows several scans in the low temperature range.

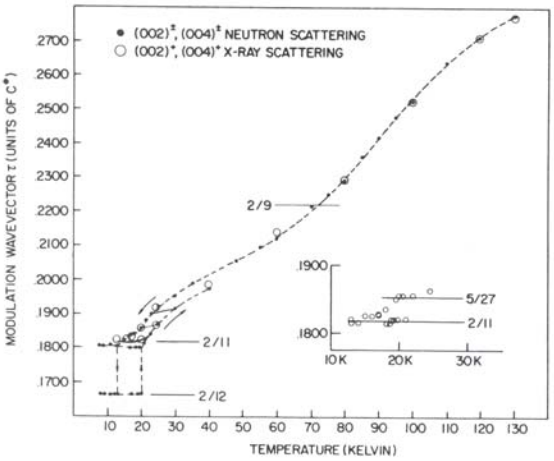

Fig. 18: *The temperature-dependent magnetic modulation wavevector of holmium from x-ray and neutron data according to [4].*

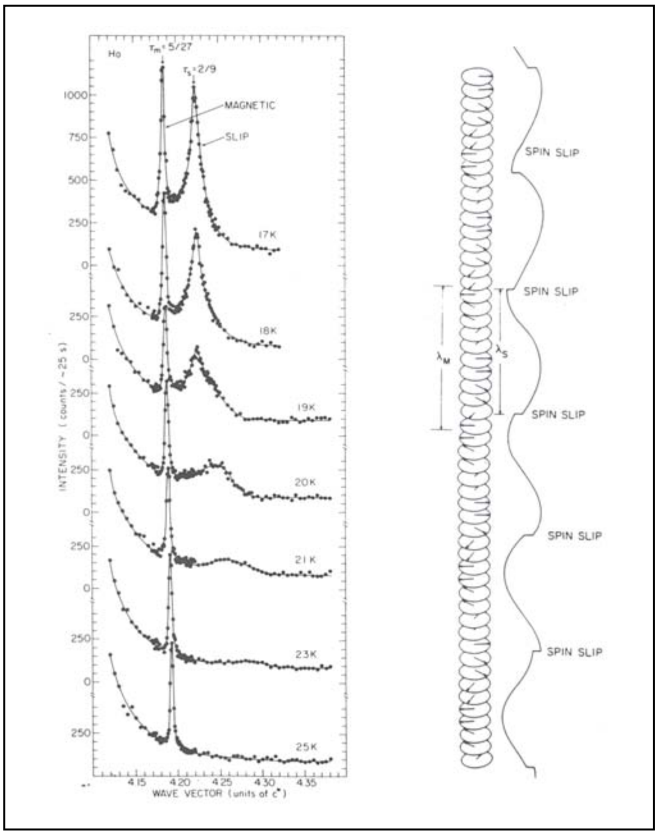

Fig. 19: *Magnetic and lattice modulation diffraction peaks in holmium at various temperatures (taken from [34]). The diagram on the right illustrates the model for magnetic ordering that can describe the observations.*

A consistent model that can describe these observations assumes the existence of discommensurations. The spin slip structure depicted on the right of figure 19 results from a competition between exchange energy and the sixfold basal plane anisotropy. According to this model, the basal plane anisotropy determines the orientation of the magnetic moment of two adjacent layers, which adopt a parallel magnetisation. The magnetisation of the next double layer is rotated by 60° and lies again along an easy in-plane axis. This pattern repeats until at one point exchange energy wins and a spin slip is introduced with only one layer and not a double layer pointing along the easy axis. The change in magnetoelastic coupling at spin slip sides causes a small distortion of the chemical lattice, with a period equal to the spin slip period λ_S. As figure 19 shows, the magnetic period λ_M and the spin slip period λ_S are different, giving rise to the two peaks observed. While the magnetic period is long range ordered, the broad charge peak indicates that the spin slip structure is short ranged with a finite correlation length. With this spin slip model, Bohr et al. [34] could calculate the allowed wavevectors for magnetic and spin slip scattering and there is a remarkable agreement with the experimental data. We do not want to discuss this example in more detail, but conclude that the high resolution of magnetic x-ray scattering compared to magnetic neutron scattering immediately gave rise to a much deaper understanding of magnetic structures and interactions in rare-earth metals.

The second example we want to discuss deals with the separation of spin and orbital angular momentum in the monoxides of 3d transition metals [36] and we have selected in particular the example of NiO [20]. Why are we interested in these very simple compounds? After all, MnO was the first material for which the antiferromagnetic structure has been determined with neutron scattering, a main corner-stone for the nobel prize of Cliff Shull. The reason is that electron correlation effects become particularly obvious in the transition metal oxides. Prominent examples of systems, which cannot be described in a simple Fermi liquid picture are the high T_C cuprates or the colossal magnetoresistance manganites, which show some very interesting and unexpected behaviour, due to electron correlations. MnO, FeO, CuO, CoO and NiO can thus be seen as test samples for band theory models. In the most simple electronic band model, the oxygen p-states are fully occupied, while the metal s-states are empty and the d-states are partially occupied. With such a picture, one would expect a partially filled band at the Fermi level, i. e. the oxides would be expected to be conductors. In reality, they show insulating behaviour, which cannot be reproduced by simple density functional theory. Moreover it is common believe that the strong crystal field on the 3d orbitals leads to a suppression of the orbital momentum, the so-called quenching. For these reasons, it is of interest to perform a separation of spin- and orbital moment magnetisation density in NiO. We have already mentioned that this is possible, when discussing the amplitude (6) of non-resonant magnetic scattering.

NiO has the NaCl fcc-structure with a = 4.177 Å at room-temperature. The ground state configuration of the Ni^{2+} ion has the $3d^8$ configuration. Below $T_N = 523$ K, NiO orders in the type II antiferromagnetic structure, where ferromagnetic planes are stacked antiferromagnetically along the [111] axis with their magnetic moments, aligned in the [111] planes, along one of the $\left[11\bar{2}\right]$ directions. The magnetic structure of MnO is depicted in figure 20.

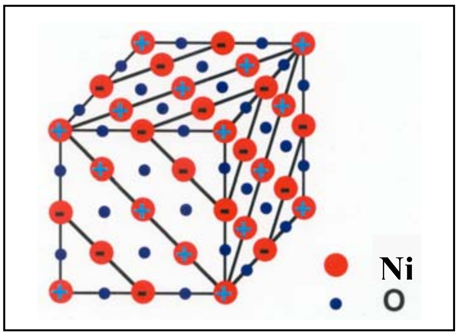

Fig. 20: *Magnetic unit cell of NiO.*

The separation of spin and orbital contributions can be done by means of polarisation analysis. Here, we assume that the radiation incident on the sample is fully polarised in the horizontal plane. In the actual experiment, performed at the magnetic scattering beamline ID20 at ESRF, the degree of polarisation in the horizontal plane was found to be 99.5 %. As mentioned in the section on experimental considerations, pyrolytic graphite is an ideal material to be used as a polarisation analyser. In the actual experiment, PG006 was used and the incident beam energy was tuned to 7.84 keV to fulfill the 90° reflection condition at the analyser crystal. A crystal was prepared with a [111] face. Specular magnetic reflections (1/2 1/2 1/2), (3/2 3/2 3/2) and (5/2 5/2 5/2) could be measured as a function of the angle of rotation ψ around the scattering vector. The scattered magnetic intensity depends on this angle ψ since during rotation we change the components of $\underline{S}$ and $\underline{L}$, which enter the scattering cross section. Before we proceed with the discussion of the results, we have to give some explanation about the magnetic domain structure that can develop in such a crystal as it is cooled from the cubic paramagnetic phase into the orthorhombic antiferromagnetically ordered low temperature phase. Since in the cubic phase 4 symmetric equivalent [111] directions exist ([111], [$\bar{1}$11], [1$\bar{1}$1], [11$\bar{1}$]) the magnetic propagation vector can align along one of these directions. Therefore during cooling down, the crystal will be spontaneously develop 4 so-called K-domains corresponding to the symmetry equivalent [111] directions, which can be realised in different parts of the crystal. In addition the magnetic moments are aligned in the [111] planes along one of the [11$\bar{2}$] directions. Since in the cubic state, the [111] axis is a three-fold symmetry axis, there exist three equivalent possible spin directions perpendicular to the [111] axis, the so-called S-domains. Depending on crystal faults (surfaces, small angle grain boundaries, impurity atoms etc.), but also on random processes, an arrangement of these K- and S-domains develops in the sample in the low temperature phase. During the experiment it turned out that the sample just developed a single K-domain with propagation vector parallel to the surface normal, at least in the near surface region of roughly 40 micrometer probed in the experiment. However, when measuring the scattered intensities from a given K-domain, all contributions from the associated S-domains add incoherently. The S-domain distribution within a K-domain can be studied by rotating the sample about the surface normal. Such an experiment is shown in figure 21.

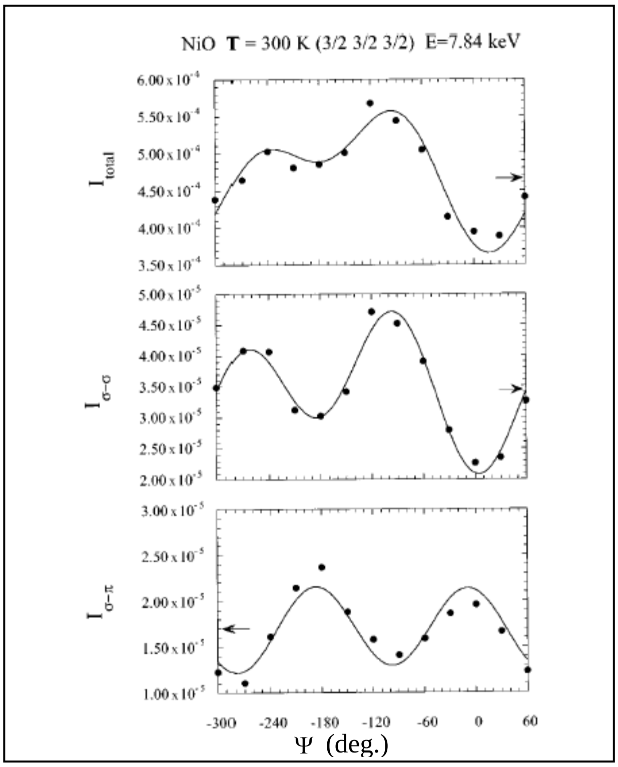

Fig. 21: *Normalised integrated intensities of the 3/2 3/2 3/2 reflection as a function of Renninger angle Ψ for the two polarisation states $\sigma \rightarrow \pi$ and $\sigma \rightarrow \sigma$ and the total scattering, respectively (from 20).*

From such experiments, the L/2S ratio can be determined. It is plotted in figure 22 as a function of sinθ/λ.

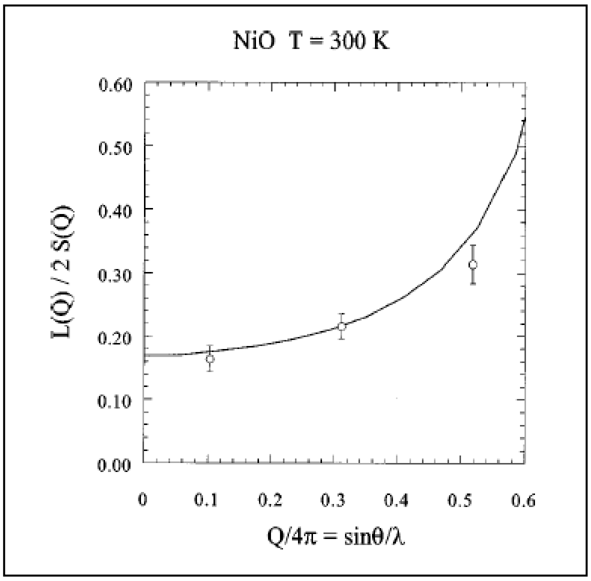

Fig. 22: *Measured variation of L(Q) / 2 S(Q) as a function of $\sin\theta/\lambda = Q/4\pi$. The continuous line is the dependence estimated from theory, adjusted to fit through the data with a contraction of the wave function by 17 % (from 20).*

By normalising to the charge reflections, the spin and orbital formfactors can be determined. They are depicted in figure 23.

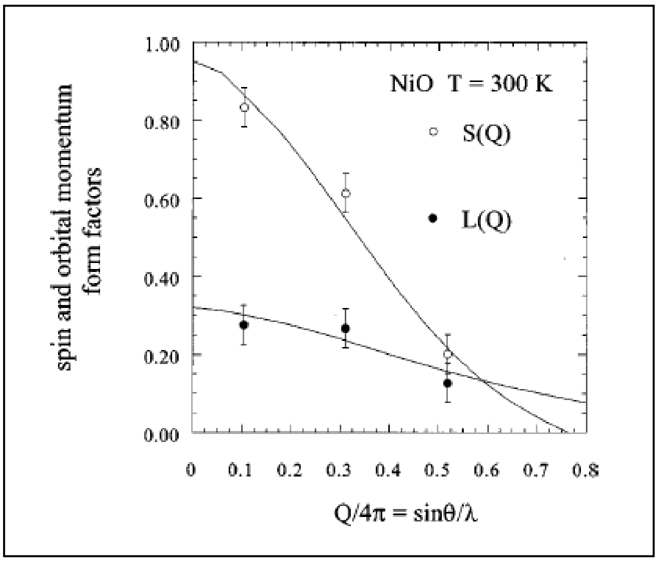

Fig. 23: *Spin and orbital moment form factors of NiO. Again the continous lines are the calculated variations of S(Q) and L(Q) with an expansion of the Q-scale by 17 % (from 20).*

Let us summarise the most important results of this investigation: First of all, there is a rather large contribution of orbital moment in NiO. In fact, the extrapolation to Q = 0 gives an effective ratio L/S = 0.34. This large contribution clearly contradicts the common believe that in such transition metal compounds, the orbital angular moment is largely quenched due to the crystal field. Furthermore, the results also indicate a contraction of the atomic wave function for Ni in NiO, if the experimental values are compared with the predictions of theory. The atomic wave functions are contracted by 17 % as compared to the free ion. We can conclude that the magnetisation density in a simple system like NiO is not yet fully understood and the results of these studies have to be taken into account, when models for the electronic and magnetic structure and properties of transition metal compounds are being made.

So far, we have discussed the magnetic scattering of x-rays in the "conventional energy range" between 4 and 20 keV. We now want to discuss an alternative method, namely the non-resonant magnetic scattering of very hard x-rays with energies above 80 keV [22-25]. From (9) it follows that with high energy x-ray diffraction one can determine the spin density distribution independent of the polarisation of the incident beam and without analysis of the final polarisation after scattering. While in neutron diffraction only the total magnetic moment, proportional to the sum L+2S is accessible, x-ray diffraction in the conventional energy range requires polarisation analysis to separate the spin momentum $\underline{S}(\underline{Q})$ from the orbital angular momentum density $\underline{L}(\underline{Q})$. The additional principal feature of high energy magnetic x-ray diffraction is the drastic increase in penetration depth. For 3d transition metals, the absorption length $1/\mu$ increases from some µm at 8 keV to several mm at 80 keV. This leads to a volume enhancement of the signal which is, however, partly compensated by the λ^2 term for the reflectivity. Moreover, true bulk properties become accessible, a feature especially important for studies of magnetic disorder phenomena. Magnetic x-ray scattering can be studied in transmission geometry. Corrections for absorption, extinction, beam foot print etc. are simple and therefore, by normalising the intensity of the magnetic reflections to the intensity of the charge reflections, absolute values for the spin moment can be determined [25]. Neutron and photon experiments of bulk properties from the same crystal become possible, where one advantage of the x-ray study is the high intrinsic resolution of about 10^{-3} Å^{-1} longitudinal and $2\cdot10^{-4}$Å^{-1} transversal.

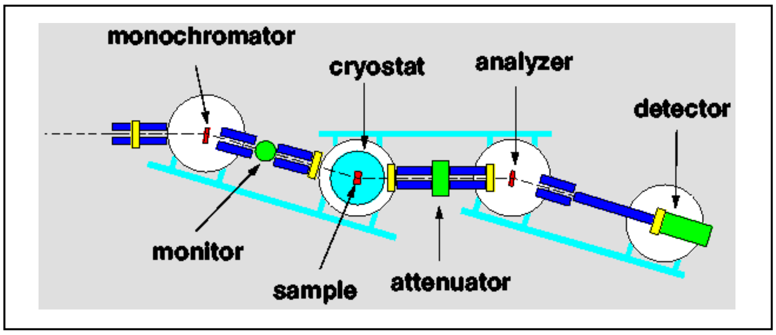

Fig. 24: *Schematic sketch of the three crystal diffractometer for high energy x-ray scattering BW5 at HASYLAB/Hamburg (http://www-hasylab.desy.de).*

Figure 24 depicts a typical experimental set-up. The diffractometer of the beamline BW5 at HASYLAB receives a white x-ray beam from a 2T high field wiggler. Inclined water cooled Cu plates limit the beam dimensions to about 4 x 4 mm^2. To reduce the heat load on the optical elements, a water cooled 1 mm thick Cu window absorbs all radiation of energy smaller than 60 keV. For the experiments on MnF_2 described below, we employed annealed Si 311 crystals with a mosaic width of 10´´ in Laue (transmission) geometry as monochromator and analyser crystals. The analyser can be used to increase the momentum space resolution and to reduce the background, but should not be employed for the collection of integral intensities. Iron collimators with a quadratic cross section of 50 x 50 mm^2 and a free bore of 10 x 10 mm^2 are positioned between monochromator and sample, sample and analyser and analyser and detector to reduce the background. With an energy sensitive Ge solid state detector, the inelastic background from Compton scattering and fluorescence can be efficiently suppressed. The sample is mounted inside a cryostat with Al windows and large tails to avoid Al background scattering to enter the detector.

The potential of magnetic high energy x-ray diffraction can be demonstrated with experiments on the antiferromagnetic model system MnF_2 [24]. Its structure is shown in figure 25. With an energy of 80 keV, a high peak count rate of 12.000 counts/sec, a good peak-to-background ratio of 230:1 and an excellent Q space resolution can be obtained for the magnetic 300 Bragg reflection. Figure 26 shows a measurement of the temperature dependence of the sublattice magnetisation. In the critical region close to the Néel temperature T_N, the reduced sublattice magnetisation $m = M(T)/M(T=0)$ follows very accurately a power law behaviour

$$m(\tau) = D \cdot \tau^{\beta} \tag{23}$$

as a function of the reduced temperature $\tau = (T_N - T)/T_N$. The value of the critical exponent of β=0.333(3) corresponds well to the predictions of the Ising model.

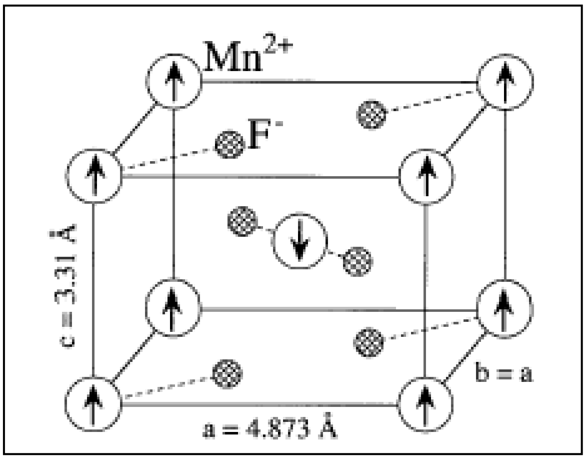

Fig. 25: *The crystalline and magnetic unit cell of MnF_2.*

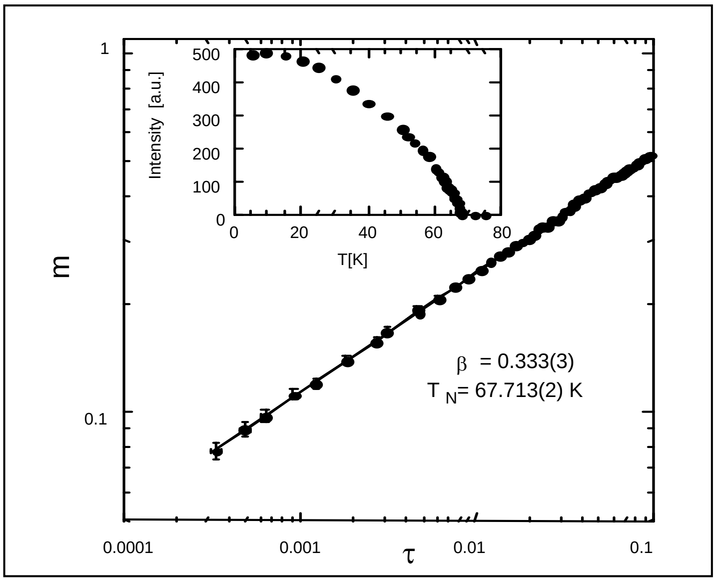

Fig. 26: *Critical behaviour of the sublattice magnetisation of MnF_2 in a double logarithmic plot in reduced variables. The insert shows the temperature dependence of the intensity of the magnetic 3 0 0 Bragg reflection of MnF_2 measured with 80 keV photons.*

MnF_2 is a classical model antiferromagnet with localised spin moments and therefore is an ideal test material for any new technique in magnetism. The 3d metal Cr on the other hand shows very intriguing magnetic properties. Chromium is an itinerant antiferromagnet exhibiting an incommensurate spin density wave (SDW) below $T_N = 311$ K [26]. Above the spin flip transition at $T_{SF} = 123$ K the spin density wave is transversally polarised, whereas below T_{SF} the polarisation becomes parallel to the modulation wave vector, which leads to a longitudinally polarised SDW. The SDW gives rise to magnetic satellite peaks at positions corresponding to the magnetic propagation vector q_m. These satellites could be readily measured, despite the small root-mean-squared moment of 0.43 μ_B, see figure 27. The temperature dependence of the intensity and propagation vector for the $1-\delta\ 0\ 0$ satellite is plotted in figure 28. One can clearly see the spin flip transition at 123 K in a drastic drop of the satellite intensity as the spin moment rotates from an orientation perpendicular to the scattering plane to an orientation within the scattering plane. Therefore at the spin flip transition, the spin component S_2 - and according to (9) the Bragg intensity - vanishes.

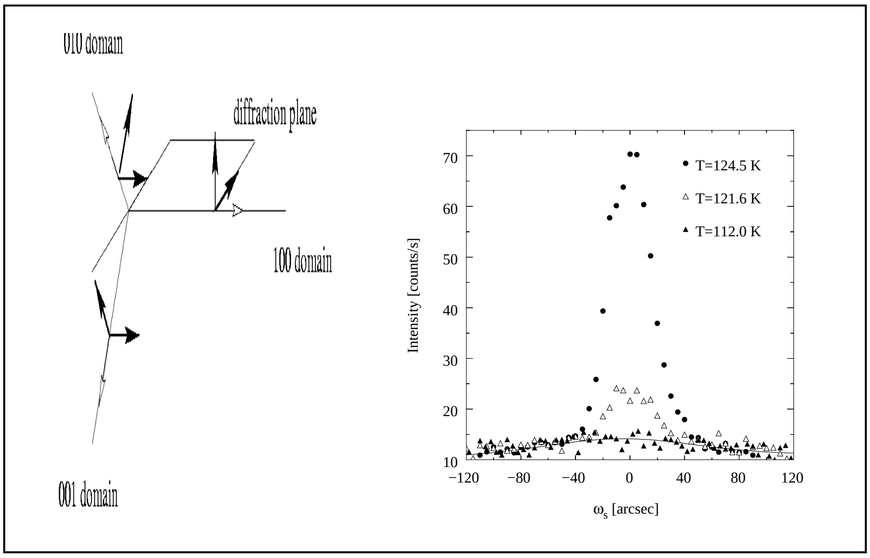

Fig. 27: *Diffraction geometry (left) and 1-δ00 magnetic satellite (right) of Cr. The measurements were done with photons of energy 100 keV. While above the spin flip transition in the transverse SDW, moments perpendicular to the diffraction plane exist, these moments come to lie within the diffraction plane as the SDW becomes longitudinal polarised below T_{SF}.*

The main aim of our study of chromium was, however, to determine the relative contribution of spin and orbital angular momentum to the SDW. As discussed above, the spin momentum is directly accessible with high energy x-ray diffraction, while neutrons measure the combination L+2S. Therefore by combining results of measurements of both techniques, spin S and orbital L momentum densities can be determined separately. To this end, we measured 5 satellites of Cr as a function of momentum transfer. In figure 29 we compare these high energy x-ray data with neutron results of Moon et al. [27]. In addition, results of calculations using a fully relativistic spin density functional theory for the form factors of spin and orbital angular momentum are shown. Neutron and x-ray data coincide within the error bars indicating a magnetic moment due to spin only. This interpretation is supported by the band structure calculation. A more detailed analysis gives an orbital contribution of -4(8)%. It is interesting to note that the orbital moment for antiferromagnetic chromium is about an order of magnitude smaller than that calculated for the pure ferromagnetic transition metals Fe, Co and Ni.

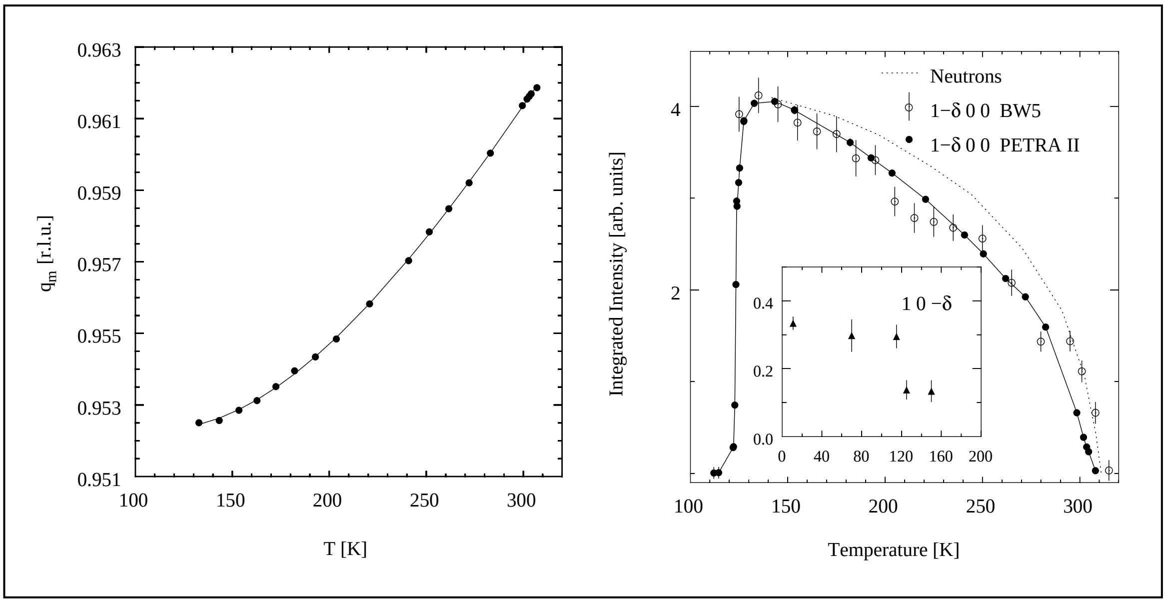

Fig. 28: *Temperature dependence of the magnetic propagation vector (left) and of the intensity (right) of the $1-\delta\ 0\ 0$ magnetic satellite of Cr measured with photons of energy 100 keV.*

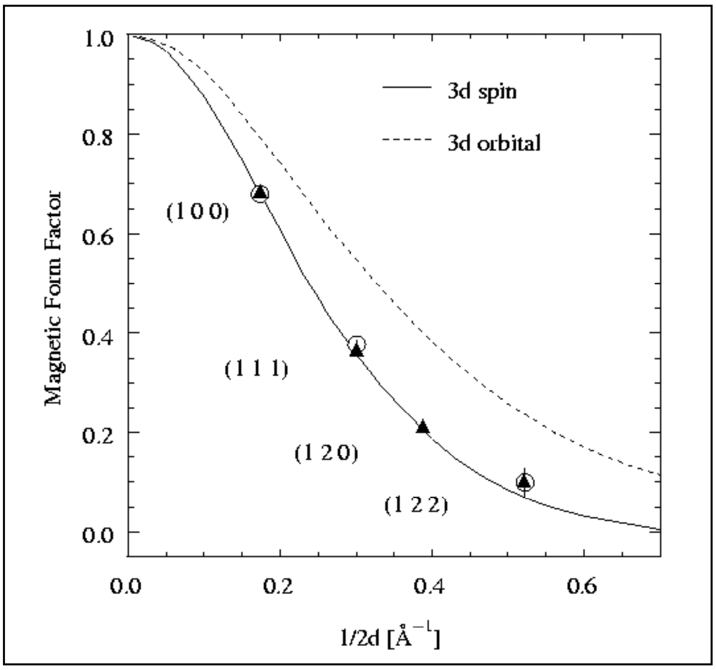

Fig. 29: *Magnetic form factor of Cr in the ordered state as a function of momentum transfer (respectively 1/2d, where d denotes the lattice spacing). Full triangles are neutron results on a commensurate Cr alloy [27]. Open circles correspond to averaged values from magnetic satellites around the commensurate positions determined with 100 keV high energy x-rays.*

6 Summary; comparison to magnetic neutron scattering

The above examples clearly demonstrate that x-ray diffraction from magnetic materials has become a microscopic probe of magnetism, complementary to the traditional probe of neutron scattering. First, it allows the investigation of strongly neutron-absorbing materials, e. g. GdS and EuS. Second it stands out by the high momentum-space resolution of typically 10^{-4}Å^{-1}, about one to two orders of magnitude better than a standard neutron experiment. This is of advantage for the investigation of incommensurate structures (e.g. Ho or Cr), magnetic disorder phenomena which involve a broadening of the magnetic Bragg reflection or critical scattering. In critical scattering investigations of the sublattice magnetisation, the magnetic Bragg peak can be well separated from critical diffuse scattering (see our example of MnF_2). For measurements of the critical diffuse scattering, the high Q-space resolution permits a detailed line shape analysis and a closer approach of the phase transition. Moreover, due to the high incident energy the full integration over the energy spectrum of magnetic fluctuations is guaranteed. Third, x-ray diffraction is a perfect tool for the investigation of surface-near phenomena and ultimately of surface magnetism [33, 18].

Considering non-resonant and resonant scattering, some specific applications are opened for each technique. In the case of resonance-exchange scattering, most evidently the resonance-enhancements at the absorption edges allow the investigation of samples with very small magnetic moments. A „magnetic“ spectroscopy of the unoccupied levels above the Fermi edge is possible (compare the discussion of the scattering from EuS). Finally the resonance effects render magnetic scattering element specific. In alloys and mixed crystals it is now possible to investigate the magnetic order of the various magnetic elements separately. In addition to the sensitivity to the magnetic species, a sensitivity to the electronic states can be achieved (compare the Er/Tb multilayer). The big draw back of resonant scattering is, however, that as for any second order perturbation process the scattered intensity is not easily interpretable in a simple and fundamental quantity such as the magnetic moment. This is one reason, why non-resonant scattering remains essential. It permits the separate determination of the spin- and angular moment contributions to the form factor. The rich cross section of non-resonant scattering gives complementary information to neutron diffraction in the case of complicated magnetic structures. As a special case of non-resonant scattering we introduced the diffraction of high-energy x-rays with energies around or above 100 keV. The large penetration power makes this radiation a true volume probe just like neutron scattering. A simple sample environment without specific x-ray transparent windows can be used and x-ray and neutron diffraction experiments can be performed from the same bulk crystal. A volume enhancement of the signal is obtained, independent of composition. The short wavelength and the small cross section eliminate extinction effects, which allows precision measurements of structure factors within the first Born approximation. Finally, the simple form of the cross section (9) makes possible a mapping of the spin momentum distribution alone without polarisation analysis and by combination with neutron diffraction, a determination of $L(\underline{Q})$ and $S(\underline{Q})$ can be achieved.

The experimental techniques for neutron and magnetic x-ray scattering are similar in many ways. For both techniques, polarisation analysis allows the separation of magnetic from non-magnetic scattering. “Flipping ratio” measurements are employed for both probes to measure the interference effects between magnetic and non-magnetic contributions.

There are, of course, clear differences between the three probes:

- For neutron scattering, nuclear and magnetic scattering are comparable in magnitude, while for x-ray scattering the magnetic contribution is generally significantly smaller. Therefore, magnetic structure determination from powder samples will remain a typical task for neutron scattering.
- The form factors are quite different for the three techniques: In XRES, the spatial extension of the core levels is relevant and therefore virtually no decrease of the scattering amplitude as a function of momentum transfer is observed. In non-resonant x-ray scattering, the form factors of spin and angular momentum can be determined separately, while neutrons are sensitive to a combination of both.
- Angular- and polarisation dependencies are richer for magnetic x-ray scattering. To give an example: magnetic neutron scattering is sensitive only to the magnetic moment perpendicular to the scattering vector Q, while x-rays see various components of $\underline{L}$ and $\underline{S}$, compare (6).
- Due to small cross section for magnetic x-ray scattering, the study of magnetic excitations and fluctuations remains a domain of inelastic neutron scattering

To summarise: both neutron and x-ray scattering techniques are important for the investigation of magnetic structures. They are largely complementary and it is wise for every condensed matter scientist to know the strengths and weaknesses of both methods and to chose carefully which probe to use to solve a specific problem in magnetism.

References

[1] P. M. Platzman and N. Tzoar, Phys. Rev. B9, 3556 (1970)

[2] F. de Bergevin and M. Brunel, Phys. Lett. A39 , 141 (1972)

[3] F. de Bergevin and M. Brunel, Acta Cryst. A37 , 314 (1981)

[4] D. Gibbs, D. E. Moncton, K. L. D'Amico, J. Bohr and B.H. Grier, Phys. Rev. Lett. 55, 234 (1985)

[5] D. Gibbs, D. R. Harshman, E. D. Isaacs, D. B. McWhan, D. Mills and C. Vettier, Phys. Rev. Lett. 61, 1241 (1988)

[6] P.M. Platzman and N. Tzoar, Phys. Rev. B9, 3556 (1970)

[7] M. Blume, J. Appl. Phys. 57, 3615 (1985)

[8] M. Blume and D. Gibbs, Phys. Rev. B37, 1779 (1988)

[9] H. Grotch, E. Kazes, G. B. Matt and D. A. Owen, Phys. Rev. A27, 243 (1983)

[10] S. M. Durbin, Phys. Rev. B57 , 7595 (1998)

[11] M. Blume in G. Materlik, C. J. Sparks and K. Fischer, Resonant Anomalous X-Ray Scattering, 495 (North-Holland, Amsterdam, 1994)

[12] J. P. Hannon, G. T. Trammell, M. Blume and D. Gibbs, Phys. Rev. Lett. 61(1988), 1245 and Erratum: Phys. Rev. Lett. 62, 2644 (1989)

[13] A. Stunault, F. de Bergevin, D. Wermeille, C. Vettier, Th. Brückel, N. Bernhoeft, G. J. McIntyre and J. Y. Henry, Phys. Rev. B60 , 10170 (1999)

[14] H. A. Dürr, E. Dudzik, S. S. Dhesi, J. B. Goedkoop, G. van de Laan, M. Belakhovsky, C. Mocuta, A. Marty and Y. Samson, Science 284 , 2166 (1999)

[15] Th. Brückel, D. Hupfeld, J. Strempfer, W. Caliebe, K. Mattenberger, A. Stunault, N. Bernhoeft and G. J. McIntyre, Eur. Phys. J B19, 475 (2001)

[16] C. Schussler-Langeheine, E. Weschke, A. Y. Grigoriev, H. Oh, R. Meier, D. V. Vyalikh, C. Mazumdar, C. Sutter, D. Abernathy, G. Grübel and G. Kaindl, J. Electron. Spectrosc. 114, 953 (2001)

[17] E. D. Isaacs, D. B. McWhan, C. Peters, G. E. Ice, D. P. Siddons, J. B. Hastings, C. Vettier and O. Vogt, Phys. Rev. Lett. 62, 1671 (1989)

[18] S. Ferrer, P. Fajardo, F. de Bergevin, J. Alvarez, X. Torrelles, H. A. von der Vegt and V. H. Etgens, Phys. Rev. Lett. 77, 747 (1996)

[19] J. P. Hill and D. F. McMorrow, Acta Cryst. A52, 236 (1996)

[20] V. Fernandez, C. Vettier, F. de Bergevin, C. Giles and W. Neubeck, Phys. Rev. B57, 7870 (1998)

[21] D. Mannix, P.C. de Camargo, C. Giles, A.J.A. de Oliveira, F. Yokaichiya and C. Vettier, Eur. Phys. J. B20, 19 (2001)

[22] Th. Brückel, M. Lippert, R. Bouchard, T. Schmidt, J.R. Schneider and W. Jauch, Acta Cryst. A49, 679 (1993)

[23] M. Lippert, Th. Brückel, Th. Köhler and J.R. Schneider, Europhys. Lett. 27, 537 (1994)

[24] J. Strempfer, Th. Brückel, U. Rütt, J.R. Schneider, K.D. Liss, and T. Tschentscher, Acta Cryst. A52, 438 (1996)

[25] J. Strempfer, Th. Brückel, D. Hupfeld, J. R. Schneider, K.-D. Liss, and T. Tschentscher, Europhys. Lett. 40, 569 (1997)

[26] J. Strempfer, Th. Brückel, W. Caliebe, A. Vernes, H. Ebert, W. Prandl, and J.R. Schneider, Eur. Phys. J. B14, 63 (2000)

[27] R. M. Moon, W. C. Koehler and A. L. Trego, J. Appl. Phys. 37, 1036 (1966)

[28] S. C. Perry, M. M. R. Costa, W. G. Stirling, M. J. Longfield, D. Mannix and Th. Brückel. J. Phys.: Condens. Matter 10, 1951 (1998)

[29] D. Hupfeld, W. Schweika, J. Strempfer, K. Mattenberger, G.J. McIntyre and Th. Brückel, Europhys. Lett. 49, 92 (2000)

[30] D. Hupfeld, W. Schweika, J. Strempfer, W.A. Caliebe, U. Köbler, K. Mattenberger, G. J. McIntyre, F. Yakhou and Th. Brückel, Eur. Phys. J. B26, 273 (2002)

[31] J. Voigt, E. Kentzinger, U. Rücker, D. Wermeille, D. Hupfeld, W. Schweika, W. Schmidt and Th. Brückel, Europhys. Lett. 65, 560 (2004)

[32] D. Hupfeld, O.H. Seeck, J. Voigt, J. Bos, K. Fischer and Th. Brückel, Europhys. Lett.. 59, 284 (2002)

[33] G.M. Watson, D. Gibbs, G.H. Lander, B.D. Gaulin, L.E. Berman, H. Matzke and W. Ellis, Phys. Rev. Lett. 77, 751 (1996)

[34] J. Bohr, D. Gibbs, D. E. Moncton, K. L. D'Amico, Physica 140a, 349 (1986)

[35] D. Gibbs, G. Grübel, D. R. Harshman, E. D. Isaacs, D. B. McWhan, D. Mills, C. Vettier, Phys. Rev. B 43, 5663 (1991)

[36] W. Neubeck, C. Vettier, F. de Bergevin, F. Yakhou, D. Mannix, L. Ranno, T. Chatterji, J. Phys. and Chem. of Solids 62, 2173 2001)

[37] Th. Brückel, M. Lippert, T. Köhler, J. R. Schneider, W. Prandl, V. Rilling, M. Schilling, Acta Cryst. A52, 427 (1996)

[38] S. P. Collins, D. Laundy, G. Y. Guo, J. Phys.: Condens. Matter 5, L637 (1993)

Index